Physiological and Molecular Plant Pathology 145 (2026) 103287

Contents lists available at ScienceDirect

Physiological and Molecular Plant Pathology

journal homepage: www.elsevier.com/locate/pmpp

Machine-learning-guided proteomic profiling reveals chitosan-modulated parasitism in the *Pochonia chlamydosporia*–root-knot nematode interaction

C.M. Berosich, M. Valverde-Urrea, J.J. Zubcoff *, L.V. Lopez-Llorca, F. Lopez-Moya

Department of Marine Science and Applied Biology, University of Alicante, Alicante, 03690, Spain

ARTICLE INFO

Keywords:
Pochonia chlamydosporia
Meloidogyne javanica
Chitosan
Machine learning
Vitellogenin
ZP-Domain
Fungal parasitism

ABSTRACT

The nematophagous fungus *Pochonia chlamydosporia* (Pc) parasitizes *Meloidogyne javanica* (MELJA) eggs, and chitosan (T8) modulates this interaction. However, the molecular mechanisms underlying this tripartite system remain poorly understood. We performed an integrative proteomic analysis of fungal and nematode responses under four conditions (Pc, PcT8, MELJA_Pc, MELJA_Pc_T8) at 24 and 96 h post-inoculation (hpi), combining differential abundance, sequence–feature clustering, phylogenetic comparisons, and machine-learning approaches. Proteome-wide analyses indicated a stimulus-dependent restructuring of Pc, with multivariate models identifying early metabolic activators and late cell wall–associated enzymes as key drivers of its temporal response. The fungal secretome was structured by functional convergence rather than evolutionary ancestry, with extracellular hydrolases and CFEM proteins dominating Cellular Component predictions. Chitosan was associated with a strong divergence in the nematode proteome, suppressing vitellogenins, ZP-domain proteins, and Piwi regulators while enhancing ATP synthase and EF1-α isoforms. Functional enrichment suggested that chitosan coincided with shifts in nematode pathways related to cytoskeletal reinforcement and chromatin activity, while fungal parasitism alone induced gene-silencing and metabolic-stress signatures. Thirteen consensus biomarkers across machine-learning models captured these shifts. Chitosan is associated with enhanced fungal parasitism, coinciding with the activation of conserved secretory modules in Pc and proteomic shifts in MELJA that involve resilience-related pathways. These findings provide a machine-learning-guided framework for identifying molecular biomarkers of nematode susceptibility and fungal parasitism under controlled *in vitro* conditions.

1. Introduction

Plant-parasitic nematodes (PPNs), particularly root-knot nematodes (RKNs) of the genus *Meloidogyne*, represent a global threat to food security due to their polyphagy and ability to manipulate host physiology [1–4]. *Meloidogyne javanica* is especially damaging to solanaceous crops and legumes [5], showing increasing virulence and synergistic interactions with other pathogens [6,7]. Consequently, there is an urgent demand for sustainable management strategies, including botanical extracts [8,9] and nanomaterials [10], as environmentally friendly alternatives to classical nematicides.

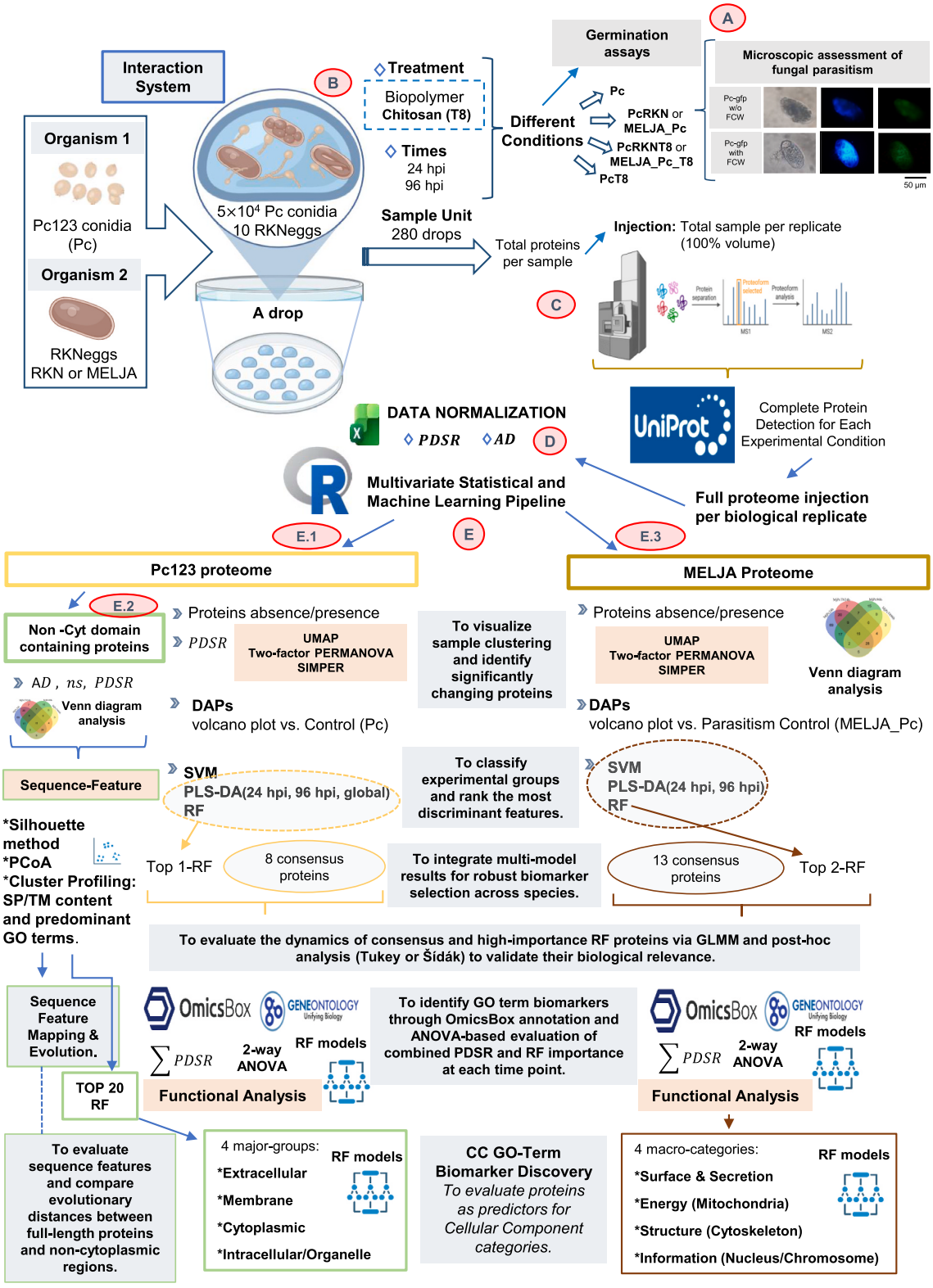
Among biological control agents, the nematophagous fungus *Pochonia chlamydosporia* (Pc) stands out for its ability to parasitise RKN eggs through appressoria formation and the secretion of a robust hydrolytic arsenal, including VCP1, chitinases, and glycosyl hydrolases [11–16]. Beyond its parasitic role, Pc colonizes roots endophytically, promoting plant growth and reducing nematode infection [17,18].

Recent evidence suggests that Pc can remodel its cell wall during infection, inducing local biosynthesis of chitosan [19]. Chitosan—a copolymer of N-acetyl-D-glucosamine and D-glucosamine—functions as a dual modulator of gene expression in plants and fungi [20]. Although typically inhibitory to phytopathogens via ROS induction [21–24], Pc exhibits resistance to chitosan due to low membrane fluidity [25]. In Pc, chitosan enhances carbohydrate metabolism, proteolysis, and redox balance [22,26], while also stimulating egg parasitism and root colonization [16,27,28]. Concurrently, chitosan activates systemic plant defences [29–31]. This multifactorial activity positions chitosan as a key molecule for exploring the physiological and molecular determinants of the Pc-nematode tripartite interaction.

Although the *P. chlamydosporia*–RKN interaction has been widely studied, the molecular signatures activated when the fungus encounters host eggs in the presence of chitosan remain largely unexplored. High-

* Corresponding author.
E-mail address: jose.zubcoff@ua.es (J.J. Zubcoff).

https://doi.org/10.1016/j.pmpp.2026.103287
Received 31 March 2026; Received in revised form 15 May 2026; Accepted 20 May 2026
Available online 1 June 2026
0885-5765/© 2026 The Authors. Published by Elsevier Ltd. This is an open access article under the CC BY-NC-ND license (http://creativecommons.org/licenses/by-nc-nd/4.0/).



(caption on next page)

Fig. 1. Multidimensional proteomic workflow for the study of the fungus-nematode interaction modulated by chitosan. (A-B) Interaction system and experimental conditions: Microscopic assessment of parasitism and germination assays of Pochonia chlamydosporia (Pc123) on Meloidogyne javanica (MELJA) eggs. The interaction was evaluated under different treatments involving the Chitosan T8 biopolymer at specific infection stages (24 and 96 hpi) to assess the differential proteomic profiling of the fungal-nematode interface. (C-D) Data acquisition and normalization: Sample analysis and abundance normalization through ***PDSR*** and ***AD*** for full proteome characterization.(E) Multivariate Statistics and Machine Learning (ML) pipeline:

- **Data exploration**: Visualization of sample clustering via UMAP and identification of Differentially Abundant Proteins (DAPs).
- **Predictive modelling**: Supervised classification of experimental groups and prioritization of discriminant features using **SVM, PLS-DA,** and **RF** algorithms.
- **Consensus analysis and validation**: Selection of robust protein candidates through multi-model integration and evaluation of abundance trends via **GLMM** with **Tukey/Šídák** post-hoc tests.
- Functional analysis: Global functional annotation using OmicsBox and identification of Gene Ontology (GO) term biomarkers based on the combined importance of ***PDSR*** and **RF** scores across time points.
- **Evolutionary and Targeted CC Analysis**: Characterization of **Sequence Features** (e.g., **SP** and **TM** regions) and **Phylogenetic Distance Contrast** between **full-length** sequences and **non-cytoplasmic** regions. Finally, **non-cytoplasmic proteins from Pc and MELJA proteins predicting GO terms** were evaluated using an RF model to classify them into four major **Cellular Component (CC)** categories to assess their specific localization and functional role.

Abbreviations: **hpi**, hours post-infection; ***PDSR***, protein detection sampling rate; ***AD***, average detection; **UMAP**, uniform manifold approximation and projection; **DAPs**, differentially abundant proteins; **SVM**, support vector machine; **PLS-DA**, partial least squares discriminant analysis; **RF**, random forest; **GLMM**, generalized linear mixed models; **SP**, signal peptide; **TM**, transmembrane regions.

resolution proteomics, reinforced by machine-learning frameworks, offers a unique opportunity to dissect these early events and identify the protein drivers of fungal development and parasitism. While *in vitro* platforms acknowledge inherent simplifications of the soil environment, they are essential for resolving specific mechanistic adjustments that guide fungal physiology during the initial stages of infection.

The objective of this study is to characterize the temporal proteomic shifts of Pc123 and determine how exogenous chitosan modulates its germination, enzymatic arsenal, and parasitic behaviour. Through a comparative proteomic approach—complemented by functional enrichment and domain-level analyses—we evaluate the molecular adjustments at 24 and 96 hpi. This work provides a robust computational and proteomic map of the Pc–RKN system under chitosan exposure, identifying key biomarkers associated with biocontrol efficiency.

2. Materials and methods

2.1. Fungal isolate, nematode material, and chitosan preparation

Pochonia chlamydosporia var. *chlamydosporia* (= *Metacordyceps chlamydosporia* var. *chlamydosporium*) isolate 123 (Pc123; ATCC MYA-4875, CECT 20929) was used in this study [32]. The fungus was maintained on corn meal agar (CMA; Becton Dickinson and Company) at 25 °C in the dark. *Meloidogyne javanica* populations were provided by Dr. Caridad Ros (IMIDA, Murcia, Spain) and maintained on susceptible tomato (*Solanum lycopersicum* Mill. cv. Marglobe). Egg masses were collected from infected roots, surface-sterilized with 1% sodium hypochlorite, washed in sterile distilled water (SDW), and stored at 4 °C until use [17]. Egg suspensions used in all assays contained the full range of developmental stages naturally present in the population.

The chitosan used was T8 (Biolog Hepe, Bremerhaven, Germany), with a molecular weight of 70 kDa and a degree of deacetylation of 80.5%. T8 powder was dissolved in 0.25 M HCl, the pH was adjusted to 5.6 with 1 M NaOH, and the solution was dialyzed against distilled water for 48 h. The final solution was sterilized at 121 °C for 20 min and stored at 4 °C [22]. All experiments were conducted using 1 mg/mL chitosan, a concentration previously shown to promote appressorium differentiation in *P. chlamydosporia* and to increase egg infection and hyphal penetration at 96 h post-inoculation [16]. Although this concentration is well-established for inducing Pc123 developmental and parasitic responses, the use of a single chitosan dose limits the ability to infer dose-dependent effects, and this constraint is now explicitly acknowledged.

2.2. Pc123 protoplast production

Pc123 or Pc123gfp [33] was cultured on CMA plates for 10 days. The margins of four colonies were excised and homogenized in a Waring blender with 50 mL potato dextrose broth (PDB; Becton Dickinson and Company) supplemented with 50 µL of a 1:1 penicillin–streptomycin solution. The suspension was incubated at room temperature for 96 h on a rotary shaker at 120 rpm. Mycelium was re-homogenized, collected on Miracloth (MilliporeSigma, Burlington, MA, USA), washed twice with SDW, divided into three portions, and transferred to 15-mL Falcon tubes containing 10 mL osmotically stabilized medium (OM buffer: 1.2 M $MgSO_4$, 10 mM $NaPO_4$, pH 5.8). Samples were centrifuged at 5000 g for 10 min at 4 °C, and the washing step was repeated twice.

Mycelium was resuspended in 7 mL OM buffer supplemented with 120 mg/mL VINOTASTE PRO (Lamothe-Abiet; pectinase, β-1,3-glucanase, and β-1,6-glucanase activities) at pH 5.8 (OME). Tubes were gently vortexed and incubated for 3 h at 37 °C at 100 rpm. An equal volume of cold ST buffer (0.6 M sorbitol, 0.1 M Tris-HCl, pH 7.0) was added, followed by centrifugation at 5000*g* for 20 min at 4 °C. Protoplasts were collected from the OME/ST interface, washed with STC buffer (1.2 M sorbitol, 10 mM Tris-HCl pH 7.5, 10 mM $CaCl_2$), centrifuged at 3000 g for 15 min at 4 °C, resuspended in 1 mL STC buffer, filtered through Miracloth, and collected in a fresh tube(S1.A1-3).

2.3. Microscopy assay of Pc123–Nematode egg interactions

To examine the role of the Pc123 cell wall during early stages of nematode egg parasitism (Fig. 1A), two co-incubation treatments were prepared in STC buffer:

1. 1×10^6 Pc123 conidia and chlamydospores per mL with 100 *M. javanica* eggs per 50 µL (RKN100), and
2. 1×10^6 Pc123 protoplasts per mL with RKN100.

Conidial viability in STC buffer was monitored for 120 h (S1.A4). Aliquots of 10 µL were collected at 0, 12, 16, 20, and 24 h (S1.A6), stained with 5 µL Calcofluor White (CFW), and examined under UV illumination (370 nm emission, 420 nm excitation) using an Olympus BH-2 fluorescence microscope. Images were captured with a Leica DFC480 digital camera. The same procedure was applied to the GFP-tagged Pc123 isolate (Pc123gfp) at 24 h (S1.A5) [17,33].

All observations were performed under controlled *in vitro* conditions to isolate early Pc–RKN egg interaction dynamics.

2.4. Pc123 germination assays

The effect of nematode eggs on Pc123 conidial germination (Fig. 1A) was evaluated in moist chambers using STC buffer or SDW on hydrophilic glass coverslips (22 × 22 mm; Menzel-Gläser, Germany) and hydrophobic polystyrene Petri dishes (140 mm; Corning Gosselin SAS, France). Conidia and chlamydospores were harvested from 14-day CMA plates using either STC buffer or SDW. Three 50-µL drops of each suspension were placed on each surface with or without 100 eggs per drop (RKN100). The experiment included all developmental stages that were present in the population in the wild (S.1B). Each drop constituted an independent experimental unit.

To assess the effect of chitosan during early pre-penetration stages, Petri dish bases were prepared with or without 1 mg/mL chitosan and inoculated with Pc123 in the presence or absence of RKN100 and RKN10 (10 eggs per drop). All treatments contained 1×10^6 conidia and/or chlamydospores per mL.

Samples were examined at 24 h using an Olympus BH-2 microscope and photographed with a Leica DFC480 camera. Conidial germination was quantified by counting conidia with a germ tube longer than the spore width across six microscopic fields per drop, with nine drops evaluated per treatment [34].

These germination assays were conducted under controlled *in vitro* conditions, allowing precise evaluation of early Pc responses to eggs and chitosan.

2.5. Pc123–Meloidogyne javanica–chitosan interaction bioassays

The interaction between Pc123, *M. javanica* eggs, and chitosan was evaluated using independent microcosms to ensure biological independence across replicates (Fig. 1B). For each assay, two polystyrene Petri dishes (140 mm) were prepared with 140 drops (50 µL each) distributed among four treatments:

1. Pc123 (Pc),
2. Pc123 + *M. javanica* eggs (Pc + RKN, PcRKN or MELJA_Pc),
3. Pc123 + chitosan (Pc + T8 or PcT8), and
4. Pc123 + *M. javanica* eggs + chitosan (Pc + RKN + T8, PcRKNT8 or MELJA_Pc_T8).

Because the objective of this study was to characterize the fungal proteomic response during parasitism, treatments with nematode eggs alone or nematode eggs exposed only to chitosan were not included, as host development in isolation fell outside the scope of the experimental design.

The Pc treatment served as the fungal control and was performed on hydrophobic polystyrene because this surface promotes appressorium development [35] and induces secretion of adhesive substances involved in early host-surface interactions [36]. These features were confirmed by microscopic examination (S.1C). The hydrophobicity of polystyrene in an aqueous environment mimics the physicochemical behaviour of soil organic matter particles, which commonly exhibit water-repellent properties and create hydrophobic microhabitats [37, 38], while maintaining the mineral conditions of sterile distilled water.

All treatments were performed in triplicate at 24 h and 96 h post-inoculation(hpi). These time points were selected to capture biologically distinct stages of the interaction: 24 hpi corresponds to early pre-penetration events, which align with our germination and microscopy assays, while 96 hpi represents a late parasitic stage at which chitosan is known to enhance egg infection and hyphal penetration. This framework also guided the deeper analysis of non-cytolytic responses.

Each drop constituted an independent experimental unit and contained 1×10^6 *Pc123 conidia and/or chlamydospores per mL*, 10 *M. javanica eggs*, and 1*mg/mL chitosan* when applicable. Egg suspensions included all developmental stages naturally present in the population (S1.B).

Because egg suspensions contained a fixed number of eggs per drop ($10\ eggs \times 280\ drops = 2,800\ eggs\ per\ replicate$), the *M. javanica* proteome represents a constant developmental pool exposed to dynamic fungal and chitosan pressures. This static input material is inherent to *in vitro* egg-based assays and provides a controlled framework for evaluating early and late nematode responses under defined microcosm conditions.

After incubation, all drops corresponding to each treatment (280 drops per replicate) were individually scraped using a fire-polished glass Pasteur pipette and collected into 15-mL Falcon tubes. To recover Pc123 germlings adhered to the polystyrene surface and to remove non-polar compounds, two additional washes were performed by scraping the dish surface with 1 mL PBS (Gibco PBS, pH 7.4) containing 1.5% Triton X-100. Wash solutions were pooled with the initial collection.

Falcon tubes were centrifuged at 5000 g for 15 min at 20 °C. Pellets were resuspended in 1 mL of the remaining supernatant and transferred to 1.5-mL Eppendorf tubes. A second centrifugation was performed at 10 000 g for 5 min at 20 °C, after which supernatants were discarded. Final pellets were stored at −80 °C until further analysis.

All assays were performed under controlled *in vitro* microcosm conditions, which allow precise manipulation of the Pc–*Meloidogyne*–chitosan interaction but do not reproduce the physicochemical complexity of natural soil environments. These simplified conditions facilitate mechanistic interpretation while limiting ecological extrapolation.

2.6. Pc123–Meloidogyne javanica interaction proteome analysis

Protein extraction, quantification, digestion, desalting, and mass spectrometry (MS) analyses were performed at the Genomics and Proteomics Unit of the University of Alicante (Fig. 1C). Pellets from all treatments were resuspended in 700 µL of water, homogenized by vortexing, sonicated using a tip sonicator, and shaken for 60 min. Total proteins were precipitated following the trichloroacetic acid (TCA)–deoxycholate (DXC) method [39]. Samples were treated with 2% (w/v) DXC, incubated at 4 °C for 15 min, and supplemented with 24% TCA. After overnight incubation at 4 °C, samples were centrifuged at 13 000 g for 10 min. Pellets were washed twice with cold 80% acetone, incubated for 10 min, and centrifuged at 14 000 g. The final precipitate was resuspended in 100 µL of 6 M urea, and protein concentration was determined at 750 nm using a bovine serum albumin (BSA) standard curve (S.2A).

For trypsin digestion, proteins were maintained in 6 M urea. Disulfide bonds were reduced with 5 µL of 0.2 M dithiothreitol (DTT) in 25 mM ammonium bicarbonate (ABC) and incubated at 37 °C for 1 h. Cysteines were alkylated with 20 µL of 0.2 M iodoacetamide (IAM) in 25 mM ABC for 60 min at room temperature in the dark. Excess IAM was quenched with 20 µL DTT, followed by addition of 100 µL 0.1 M ABC, adjusting pH to 7–9. Trypsin was added at a 1:30 (w/w) enzyme-to-protein ratio, and samples were incubated overnight at 37 °C. A second digestion step was performed by adding trypsin at a 1:60 ratio and incubating for 3–5 h at 37 °C. Digestion was stopped by acidification with 3 µL formic acid to pH 1–3, and samples were evaporated to dryness.

Peptides were resuspended in 150 µL of 0.5% trifluoroacetic acid (TFA) in 5% acetonitrile (ACN). All samples were desalted using Pierce™ PepClean™ C18 columns (Thermo Fisher Scientific), except when the total peptide amount exceeded 50 µg; in such cases, the maximum binding capacity of the column (30 µg) was loaded, ensuring that either the full sample or the maximum allowable amount was injected into the system. Columns were activated twice with 200 µL 50% ACN and equilibrated twice with 200 µL 0.5% TFA in 5% ACN. Samples were loaded in 0.5% TFA/5% ACN, washed twice with the same buffer, and peptides were eluted twice with 20 µL of 70% ACN/0.1% TFA.

Peptide mixtures were analysed by MS, and peptide sequences were identified by searching against the UniProtKB database entries corresponding to the Pc123 proteome (ID 1052797) and the genus

Table 1
Random Forest classification performance for *P. chlamydosporia* (Pc123) functional profiles. Accuracy and Out-of-Bag (*OOB*) error rates across Gene Ontology (GO) categories and time points.

Time	GO Category	OOB Error (%)	Accuracy (%)
24 hpi	BP	33.33	66.67
24 hpi	CC	25.00	75.00
24 hpi	MF	**0.00**	**100.00**
96 hpi	BP	8.33	91.67
96 hpi	CC	8.33	91.67
96 hpi	MF	8.33	91.67

Table 2
Random Forest classification performance for *M. javanica* functional profiles. Accuracy and Out-of-Bag (*OOB*) error rates for Biological Process (BP), Molecular Function (MF), and Cellular Component (CC) at 24 and 96 hpi.

Time	GO Category	OOB Error (%)	Accuracy (%)
24 hpi	BP	50.00	50.00
24 hpi	MF	**83.33**	**16.67**
24 hpi	CC	33.33	66.67
96 hpi	BP	**0.00**	**100.00**
96 hpi	MF	16.67	83.33
96 hpi	CC	33.33	66.67

Meloidogyne (ID UP000887561).

2.7. Proteome data normalization

To enable a comprehensive and comparable analysis of the total protein profiles obtained for each treatment (Fig. 1D; Datasets S3 and S4), all detected proteins were first grouped according to their predicted domains or conserved regions. Proteins from Pc123 were labelled numerically (e.g., 1, 2, 3 …), whereas proteins from *M. javanica* were labelled with the prefix "M" (e.g., M1, M2 …).

Three quantitative parameters were used to evaluate protein abundance and detection consistency across samples:

1) Number of detected proteins (***n***)

The total number of proteins detected either in a single sample (***nS***) or across all replicates of a treatment (***nT***), providing a measure of proteome complexity (S.2B).

2) Protein Detection Sampling Rate (***PDSR***)

PDSR expresses the **relative contribution of each protein's spectral intensity (*IS*$_i$)** to the **total spectral intensity of all proteins detected in the same sample (*IST*)**:

$$PDSR\ (\%) = \frac{IS_i \times 100}{\sum_{i=1}^{n_s} IS_i}$$

PDSR is a **normalized intensity metric** used for **statistical analyses and machine-learning workflows**, as it allows direct comparison of protein abundance across samples with different total protein yields.

3) Average Detection Percentage (***AD***)

AD represents the **mean relative abundance of each protein across all biological replicates**, even if detected only once. For each protein, the average intensity (*IA*) across replicates (n = 3) is normalized to the sum of all average intensities (*IAT*):

$$AD\ (\%) = \frac{IA \times 100}{IAT}$$

AD is a metric that **provides a quantitative range to measure the proportion of the mean peptide intensity relative to the total intensity across all samples.** This metric **allows establishing a threshold to evaluate the proportion of total MS-measured peptide intensity associated with the experimental detection of each protein.** *AD* was used to estimate the proportion of Pc123 proteins containing non-cytoplasmic (Non-Cyt) domains, and, in our case, to identify proteins exceeding 2% relative abundance in the Pc123 (Figure S.2D) and *M. javanica* (Figure S2E) proteomes.

Together, *PDSR* and *AD* provide a quantitative, reproducible, and biologically meaningful framework for interpreting the Pc123–*M. javanica* interaction proteomes.

2.8. Functional proteome analysis

Functional annotation of the proteins detected in each treatment was performed using OmicsBox v.3.2.4 (BioBam, Spain; http://www.biobam.com/omicsbox). Protein identifiers were matched to the UniProtKB proteomes corresponding to Pc123 (ID 1052797; S.5) and *M. javanica* (ID UP000887561; S.6). Functional characterization included InterProScan domain prediction, Gene Ontology (GO) annotation, and GO-Slim classification for all conditions in which each organism was detected.

To identify the most representative biological functions in each treatment, GO terms were filtered to retain only those representing more than 8% of the total functional annotations within each GO category (Biological Process, Molecular Function, Cellular Component). For each GO term, the total Protein Detection Sampling Rate (*PDSR*) was calcu-

Table 4
Random Forest classification performance across Cellular Component (CC) sub-categories. Evaluation of Out-of-Bag (OOB) error rates, global accuracy, and protein counts (n) for each functional compartment.

CC Category	OOB Error Rate (%)	Global Accuracy	Proteins (n)
Structure (Cytoskeleton)	73.17	0.25	24
Energy (Mitochondria)	51.67	0.50	19
Information (Nucleus/ Chromosome)	59.28	0.417	30
Surface & Secretion	79.88	0.25	13

Table 3
Mantel test correlation parameters between protein structural features and phylogenetic distances. Comparison of Spearman correlation coefficients (*r*) and significance values (*p*) across experimental scenarios for non-cytoplasmic (Non-Cyt) and full-sequence datasets.

Scenario	N Proteins	Mantel r (Non-Cyt)	p	Mantel r (Full)	P	Cophenetic Corr.	Winner	
Pc_24	45	−0.089	0.975	−0.156	0.998	0.249	Localiz (Non-Cyt)	NS
PcRKN_24	27	0.095	0.094	0.009	0.480	0.024	Localiz (Non-Cyt)	NS
PcT8_24	26	−0.079	0.869	−0.058	0.801	−0.072	Evol (Full)	NS
PcRKNT8_24	35	−0.058	0.894	0.018	0.376	0.160	Evol (Full)	NS
Pc_96	29	0.105	0.092	0.047	0.263	0.173	Localiz (Non-Cyt)	NS
PcRKN_96	49	−0.018	0.649	−0.026	0.724	0.004	Localiz (Non-Cyt)	NS
PcT8_96	216	0.021	0.045	0.005	0.321	−0.060	Localiz (Non-Cyt)	NS
PcRKNT8_96	142	0.002	0.475	0.060	0.004	0.003	Evol (Full)	**Sig**

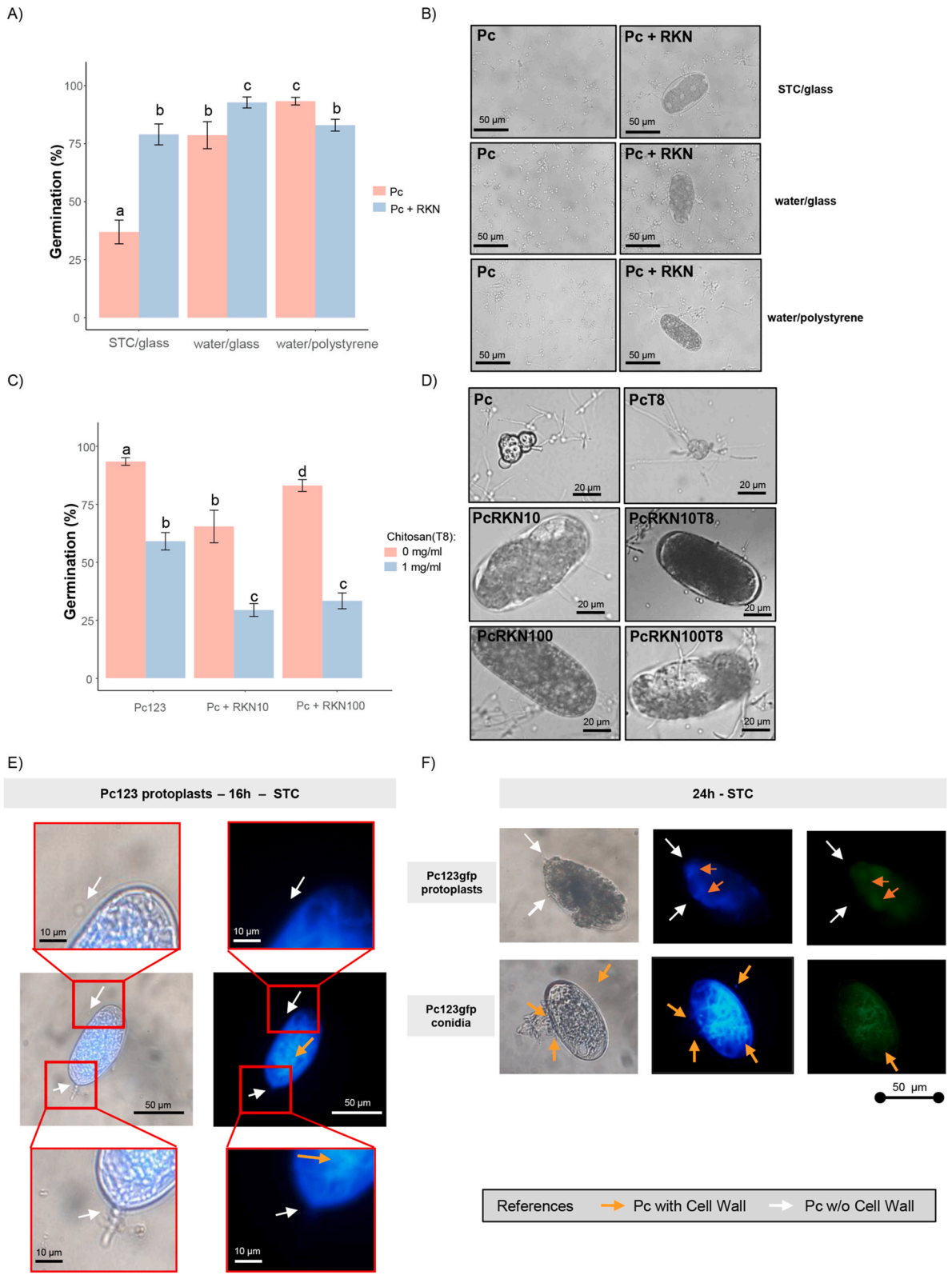


Fig. 2. Factors affecting *Pochonia chlamydosporia* (Pc123) early infection stages: surface hydrophobicity, egg-derived cues, and the role of the fungal cell wall (FCW). (A–B) Effect of surface hydrophobicity (glass vs. polystyrene) and *Meloidogyne javanica* egg presence on conidia germination at 24 hpi. **(C–D)** Inhibitory effect of chitosan (T8, 1 mg/mL) on germination and the compensatory role of increasing RKN egg densities (RKN10 and RKN100). Lowercase letters indicate significant differences ($p < 0.05$). **(E)** Microscopic visualization of Pc123 protoplasts at 16 hpi in STC buffer. Arrows indicate wall-less protoplasts (white) adhering to and penetrating the eggshell, with internal colonization preceding cell wall regeneration. **(F)** Fluorescence microscopy comparison at 24 hpi between Pc123gfp protoplasts and conidia. Protoplasts show localized adhesion and early penetration (white arrows), while conidia with intact cell walls (orange arrows) exhibit faster penetration and extensive internal colonization. Abbreviations: hpi, hours post-inoculation; RKN: root-knot nematode. (For interpretation of the references to colour in this figure legend, the reader is referred to the Web version of this article).

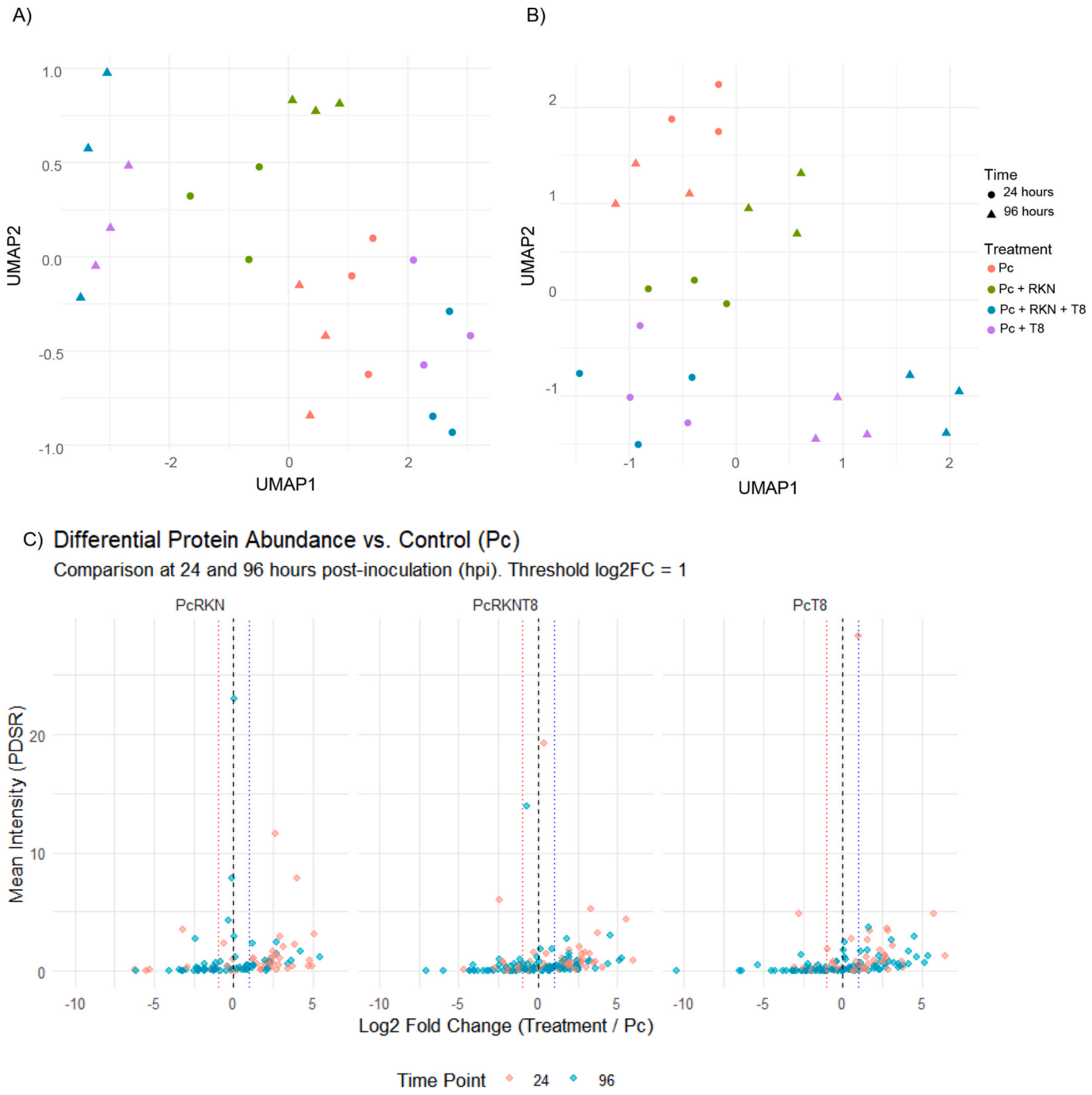


Fig. 3. Global proteomic landscape and differential abundance analysis of Pochonia chlamydosporia during interactions with Meloidogyne javanica and chitosan. A) Qualitative assessment via Uniform Manifold Approximation and Projection (UMAP) based on protein presence/absence profiles. B) Quantitative UMAP analysis based on *PDSR* values. Both projections reveal distinct clustering patterns driven by the interplay between treatment (chitosan elicitation) and sampling time (24 vs. 96 hpi). C) Volcano plots illustrating DAPs for three experimental scenarios (PcRKN, PcRKNT8, and PcT8) compared to the fungal control (Pc) at 24 and 96 hpi. Significance thresholds were set at log _2*Fold Change* > 1 and $p < 0.05$. Detailed counts of up-regulated and down-regulated proteins for each scenario are summarized in Table S.12A. Abbreviations: hpi, hours post-inoculation; Pc, P. chlamydosporia; RKN, *M. javanica*; T8, chitosan treatment; *PDSR*, protein detection sampling rate; DAPs, differentially abundant proteins.

lated by summing the *PDSR* values of all proteins annotated with that GO term in each replicate (Datasets S.7 and S.8).

2.9. Non-cytoplasmic domain protein identification and Sequence Feature analysis

Proteins predicted to contain a non-cytoplasmic (Non-Cyt) domain were identified through individual inspection of all detected proteins using the InterPro database (http://www.ebi.ac.uk/interpro). Within this group, proteins carrying a predicted signal peptide (SP) or a transmembrane region (TM) were also recorded (Dataset S.9). For each treatment, the parameters **nS** (number of detected proteins) and **PDSR** (Protein Detection Sampling Rate) were calculated for all proteins with Non-Cyt domains. A comparative overview of these proteins across treatments was generated using the Venn diagram tool from the Bioinformatics & Evolutionary Genomics platform at Ghent University

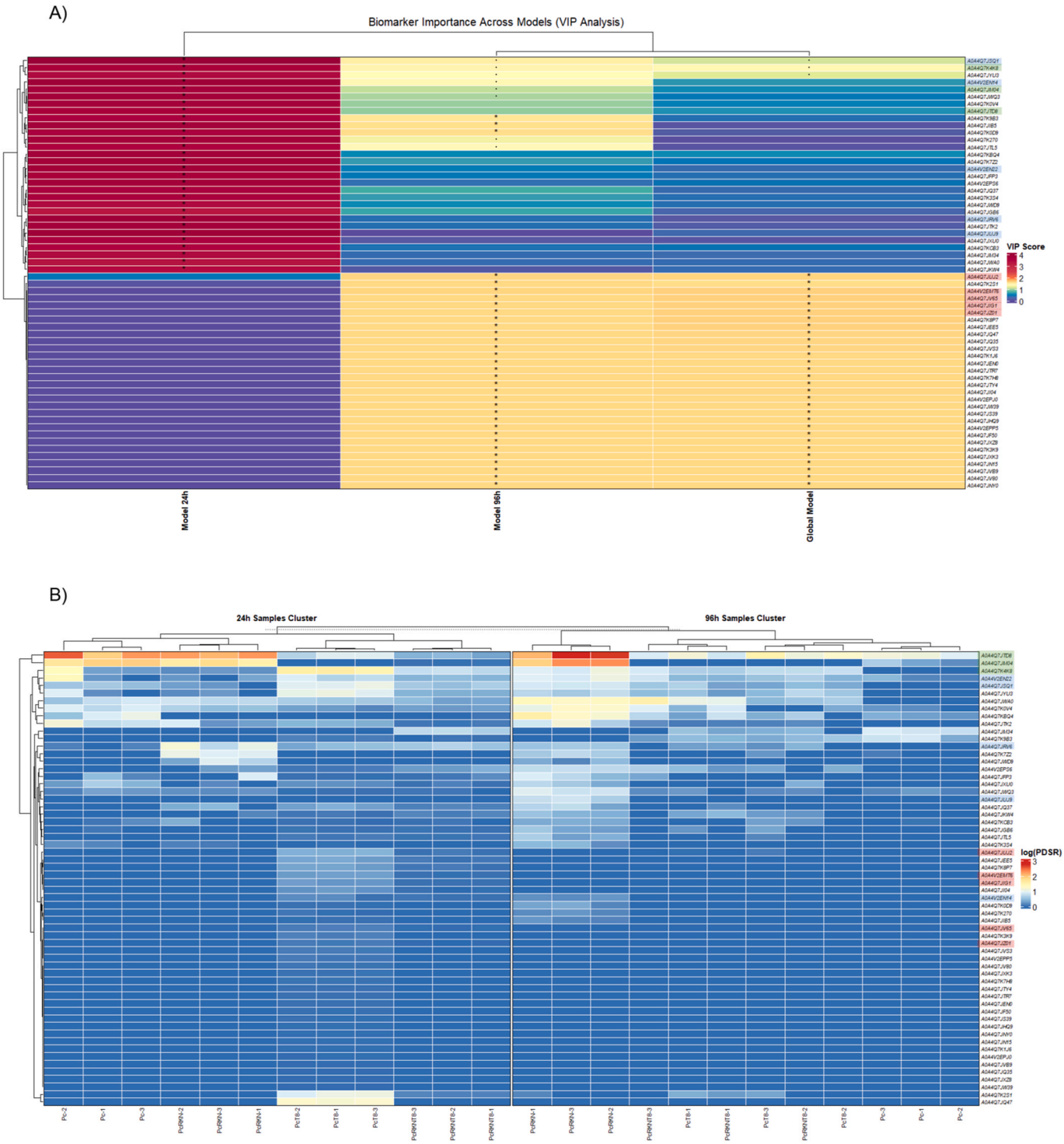


Fig. 4. Partial Least Squares Discriminant Analysis (PLS-DA) and biomarker identification in the P. chlamydosporia proteome. A) Comparison of Variable Importance in Projection (*VIP*) scores across temporal (24 and 96 hpi) and global PLS-DA models. The heatmap utilizes a Spectral-11 palette to visualize *VIP* magnitude, where markers indicate statistical significance and predictive power: asterisks (*) highlight proteins with $\boldsymbol{VIP} \geq \mathbf{1.5}$ and dots (·) indicate proteins with $\boldsymbol{VIP} \geq \mathbf{1.0}$. Hierarchical clustering was applied to the rows to assess similarity in biomarker importance among models, showing a high concordance between the global model and the 96 hpi response. B) Heatmap based on log(*PDSR*) values for the selected biomarkers. Protein IDs are color-coded to highlight key contributors: blue indicates the top 5 *VIP* proteins at 24 hpi, red denotes the top 5 *VIP* proteins at 96 hpi, and green identifies the three leading proteins in the log(*PDSR*) hierarchy. Dendrograms represent hierarchical clustering of samples, showing a clear segregation based on developmental time points (24 vs. 96 hpi). Abbreviations: *PDSR*, protein detection sampling rate; hpi, hours post-inoculation; Pc, *P. chlamydosporia*; RKN, *M. javanica*; T8, chitosan. (For interpretation of the references to colour in this figure legend, the reader is referred to the Web version of this article.)

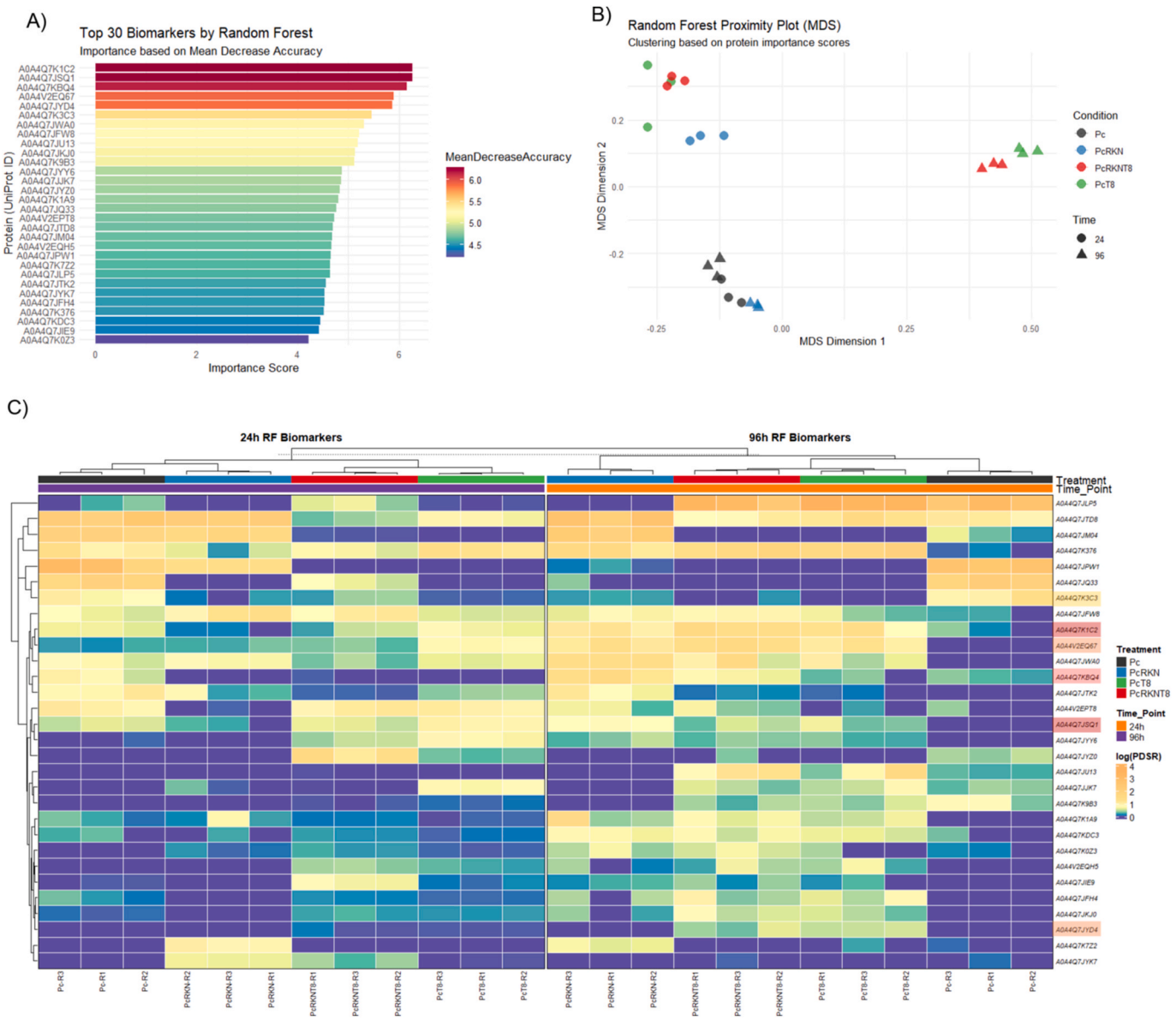


Fig. 5. Random Forest (RF) classification and identification of key proteomic drivers in *P. chlamydosporia*. A) Top 30 proteomic biomarkers ranked by Mean Decrease Accuracy. The ensemble model (1500 trees) achieved high classification performance with an Out-of-Bag (*OOB*) error rate of 20.83%. B) Multidimensional Scaling (MDS) plot based on RF proximity scores (1 − *proximity*). The projection reveals a robust spatial segregation of samples, primarily driven by the sampling time points (24 hpi circles vs. 96 hpi triangles), with treatment-specific sub-clustering. C) Hierarchical clustering heatmap of the top 30 RF biomarkers using log(*PDSR*) values and a Spectral palette. The top 6 ″lead drivers″ identified by the model are highlighted in red and orange on the Y-axis. The heatmap illustrates a clear transition in protein abundance patterns between 24 and 96 hpi, where misclassifications were minimal and restricted to specific early-stage samples (PcRKNT8 and PcT8 at 24 hpi). Abbreviations: *PDSR*, protein detection sampling rate; hpi, hours post-inoculation; Pc, *P. chlamydosporia*; RKN, *M. javanica*; T8, chitosan. (For interpretation of the references to colour in this figure legend, the reader is referred to the Web version of this article.)

(https://bioinformatics.psb.ugent.be/webtools/Venn/) (Dataset S.10).

2.10. Statistical and machine-learning analysis

2.10.1. Germination assay statistical analysis

The effect of hydrophobic conditions on Pc123 conidial germination was evaluated using a germination percentage with a two-way ANOVA, with **surface type** (hydrophilic vs. hydrophobic) and **solvent type** (SDW vs. STC buffer) as fixed factors. To assess the effect of *M. javanica* egg density and chitosan concentration on germination, a second two-way ANOVA was performed, followed by Tukey's post-hoc test for pairwise comparisons. Model assumptions were verified by testing the **normality of residuals** using the Shapiro–Wilk test and **homogeneity of variances** using Levene's test. All analyses were conducted in R version 4.3.3 [40].

2.10.2. Proteome-level statistical and multivariate analysis

Pc123 and *Meloidogyne javanica* proteins detected under all experimental conditions were analysed using both a presence/absence matrix and a detection-percentage matrix based on *PDSR* (S.11). For presence/absence data, a **Jaccard distance** matrix was computed, whereas for *PDSR* data, a **Bray–Curtis distance** matrix was calculated. Because *PDSR* values are proportions bounded between 0 and 1, a **censored logistic distribution (cld)** transformation was applied prior to distance computation. All distance-based analyses, including Bray–Curtis dissimilarities and permutation-based tests, were performed under a fixed random **seed (1234)**) to ensure full reproducibility.

To visualize global patterns in proteome composition, a **Uniform**

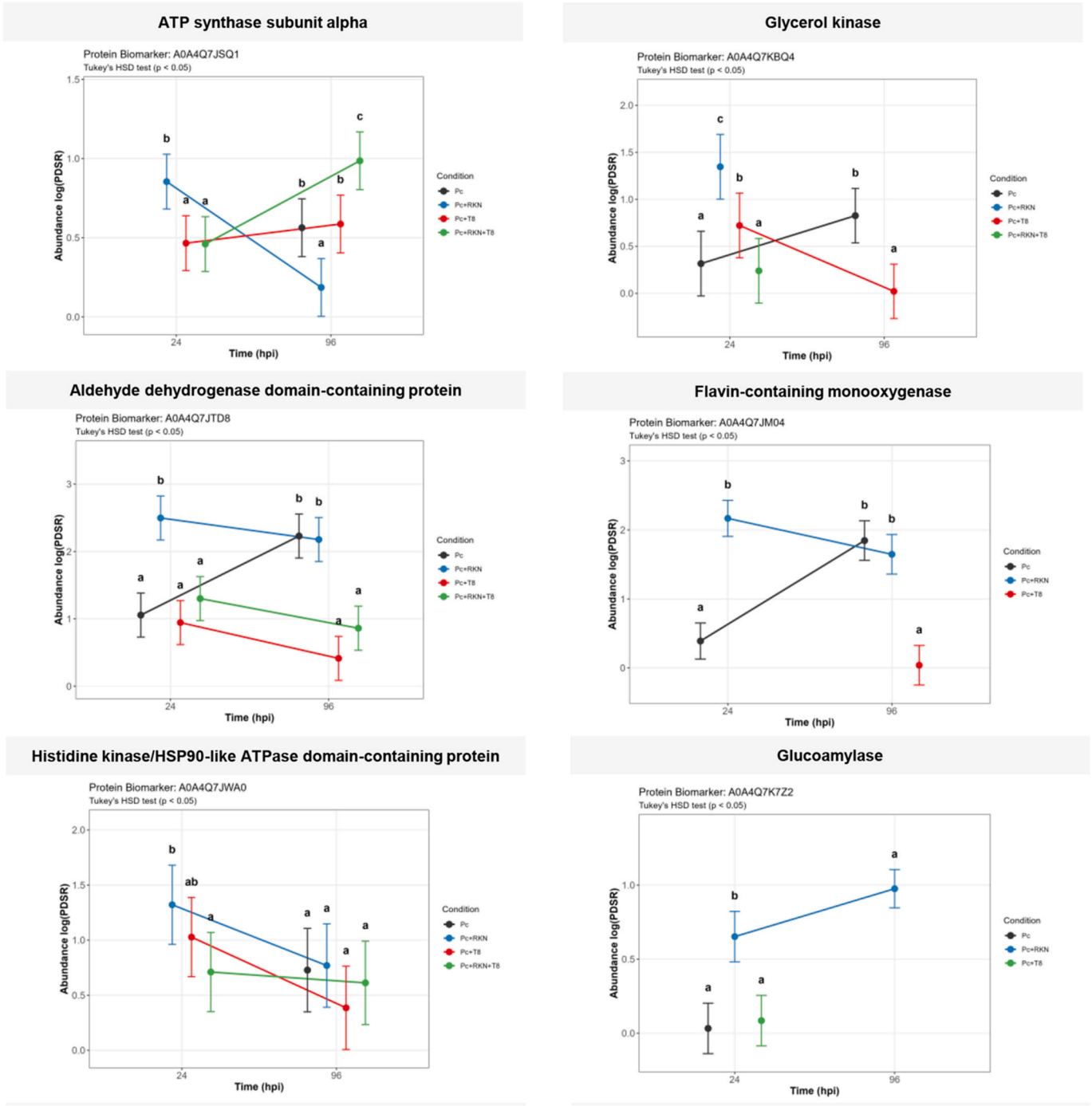


Fig. 6. Temporal abundance trends of consensus biomarkers and the lead Random Forest (RF) driver in *P. chlamydosporia*. The figure displays the abundance profiles (*log(PDSR)*) over time (24 and 96 hpi) for eight consensus proteins identified by both PLS-DA (top 60 VIP scores) and RF (top 30 Mean Decrease Accuracy) models, alongside the lead RF driver (A0A4Q7K1C2). Trend analysis was performed using Generalized Linear Mixed Models (GLMM). Lowercase letters denote significant differences according to Tukey's HSD post-hoc test ($p < 0.05$). The consensus biomarkers include key enzymes involved in energy metabolism and stress response: **ATP synthase subunit alpha (A0A4Q7JSQ1)**, which shows a significant divergence between PcRKN and chitosan-treated scenarios at 96 hpi; **Glycerol kinase (A0A4Q7KBQ4)**, exhibiting a total depletion in the presence of nematodes at 96 hpi; **Aldehyde dehydrogenase (A0A4Q7JTD8)** and **Flavin-containing monooxygenase (A0A4Q7JM04)**, which highlight specific fungal responses to RKN and control conditions; **Histidine kinase/HSP90-like ATPase (A0A4Q7JWA0)**, showing early differentiation at 24 hpi; and carbohydrate-active enzymes such as **Glucoamylase (A0A4Q7K7Z2)** and **Beta-glucosidase 1 (A0A4Q7K9B3)**. The bottom panel highlights the **Heat shock protein 70 (HSP70, A0A4Q7K1C2)**, the lead RF driver, which exhibits an early significant induction by chitosan (T8) at 24 hpi followed by a generalized decline at 96 hpi across all treatments except for the control. Abbreviations: hpi, hours post-inoculation; *PDSR*, protein detection sampling rate; PLS-DA, partial least squares discriminant analysis; *VIP*, variable importance in projection; Pc, *P. chlamydosporia*; RKN, *M. javanica*; T8, chitosan.

Manifold Approximation and Projection (UMAP) was performed using the transformed PDSR matrix. The analysis retained the **top 100 proteins** contributing most to overall variability, enabling dimensionality reduction while preserving biologically relevant structure.

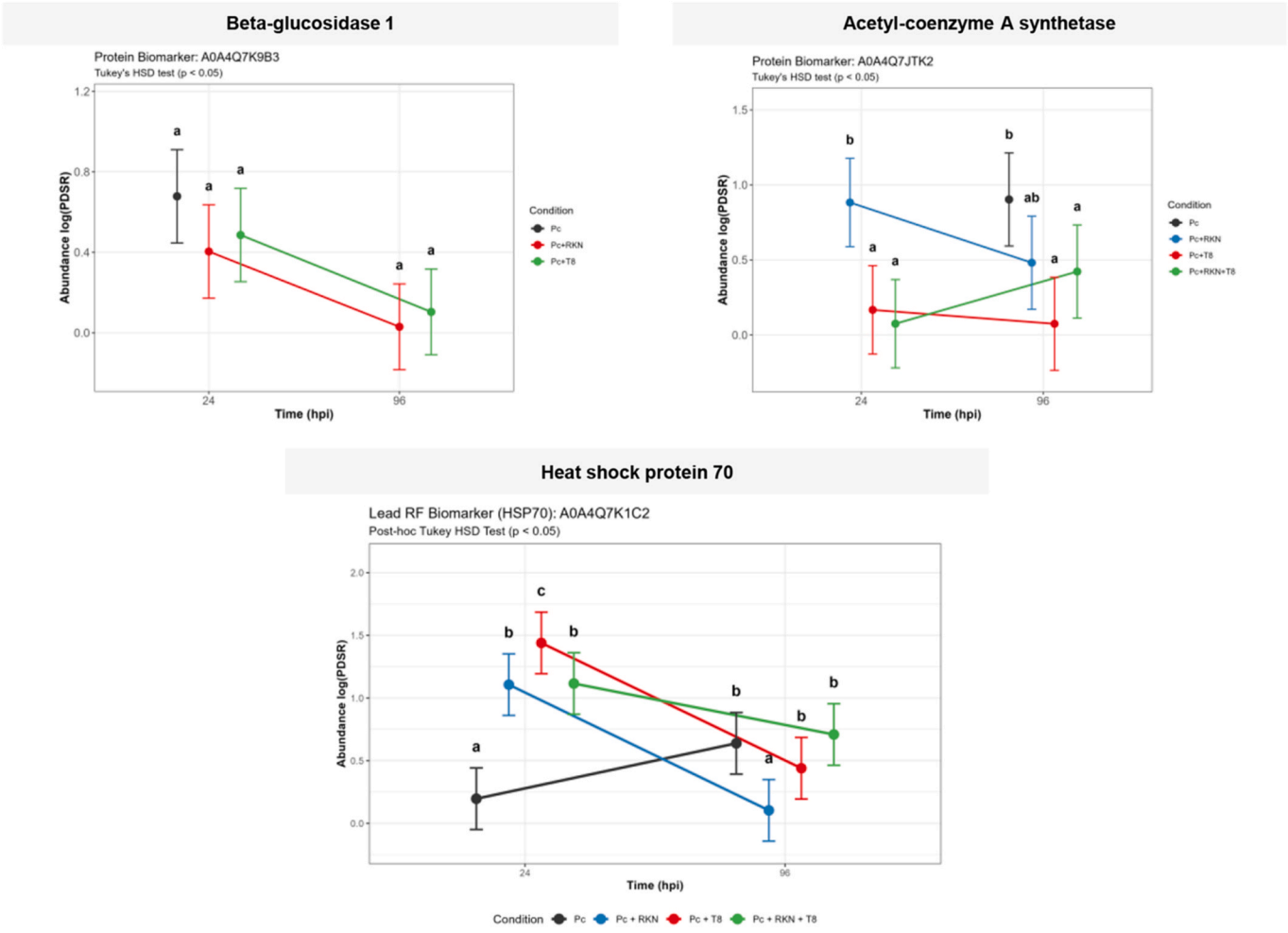


Fig. 6. (*continued*).

A two-factor **PERMANOVA** (treatment × time) was then conducted to test for significant differences in proteome composition across conditions. To identify which proteins contributed most strongly to these differences, a **SIMPER** analysis was performed. Model assumptions were evaluated by assessing the normality of residuals (Shapiro–Wilk test) and homogeneity of variances (Levene's test). All analyses were conducted in **R version 4.3.3** [40].

In addition, **Venn diagrams** of the total proteomes of Pc123 and *M. javanica* across all conditions were generated using the same platform employed for the non-cytosolic protein analysis (Bioinformatics & Evolutionary Genomics, Ghent University). These diagrams provided a comparative overview of shared and condition-specific proteins in each organism.

2.10.3. Full-proteome multivariate and machine-learning framework for Pc123

Building upon the global community-level structure characterized previously through UMAP, PERMANOVA, and SIMPER, we next applied a comprehensive suite of multivariate and machine-learning approaches to the **full Pc123 proteome** (Fig. 1E1; S.12). These analyses aimed to identify discriminant proteins, evaluate treatment- and time-dependent patterns, and extract statistically robust biomarkers for downstream interpretation.

2.10.3.1. Differential abundance analysis (volcano plot and DAPs). Differential protein abundance relative to the Pc control was evaluated using a volcano-plot framework. For each protein, mean PDSR values were calculated per condition and time point, and **$\log_2$ fold-change ($\log_2$FC)** values were computed relative to Pc. Proteins were classified as up-regulated, down-regulated, or unchanged using a $\log_2$FC threshold of ± 1. These distributions of **differentially abundant proteins (DAPs)** served as the foundation for downstream multivariate and machine-learning analyses.

2.10.3.2. Support vector machine (SVM) analysis for dataset validation. To evaluate the internal consistency and separability of the *P. chlamydosporia* proteomic dataset, a Support **Vector Machine (SVM)** classifier was implemented using a wide-format matrix of protein features (presence/absence and normalized abundance) across the eight experimental groups. A linear-kernel SVM (C-classification) was trained using the **e1071** package in R, employing **5-fold cross-validation** to ensure model robustness and direct interpretability of feature weights. Prior to analysis, protein features were scaled and the response variables were factor-encoded. This supervised learning approach served as a validation tool to confirm that biological replicates formed well-defined clusters, achieving a cross-validated accuracy of **79.2%** and 24 support vectors, thereby ensuring the reliability of the proteomic matrix for subsequent multivariate analyses.

2.10.3.3. Global PLS-DA. A global PLS-DA was performed to evaluate whether Pc123 proteomic profiles formed separable multivariate clusters across the four experimental conditions (Pc, PcRKN, PcT8, PcRKNT8) at 24 and 96 hpi. PDSR values were arranged in a wide matrix, proteins with zero variance were removed, and a log1p

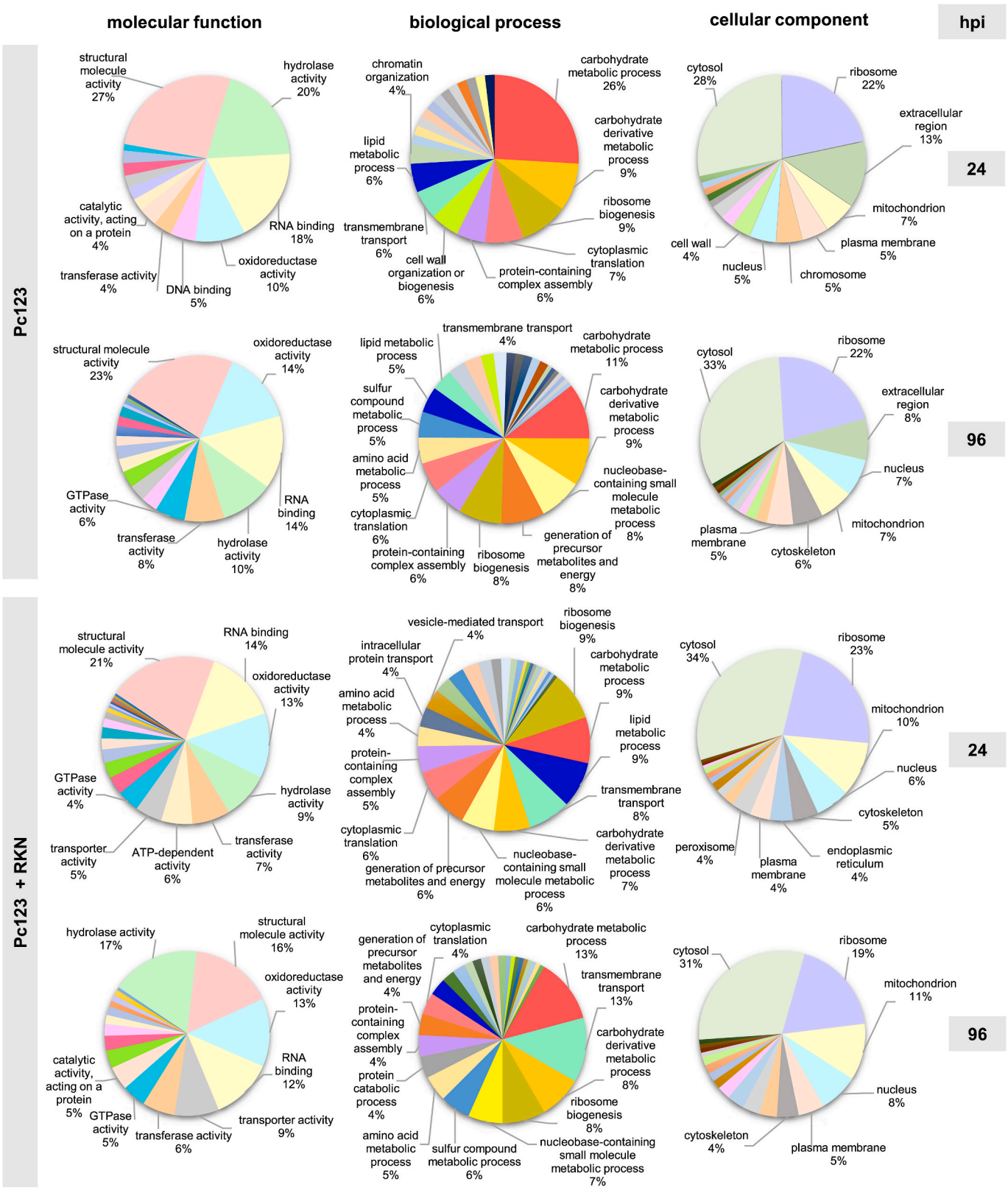


Fig. 7. Functional distribution and Gene Ontology (GO) annotation of the *Pochonia chlamydosporia* (Pc123) proteome during interaction with *Meloidogyne javanica* (RKN) eggs. The pie charts illustrate the comparative functional landscape of Pc123 in the absence (control) and presence of the nematode host. Proteins are categorized according to Biological Process (BP), Molecular Function (MF), and Cellular Component (CC). To ensure biological relevance, only GO terms representing ≥4% of the total proteome abundance are depicted. This baseline comparison highlights the primary functional shifts induced by the nematode before elicitor application. Abbreviations: hpi, hours post-inoculation; Pc123, *P. chlamydosporia*; RKN, *M. javanica*.

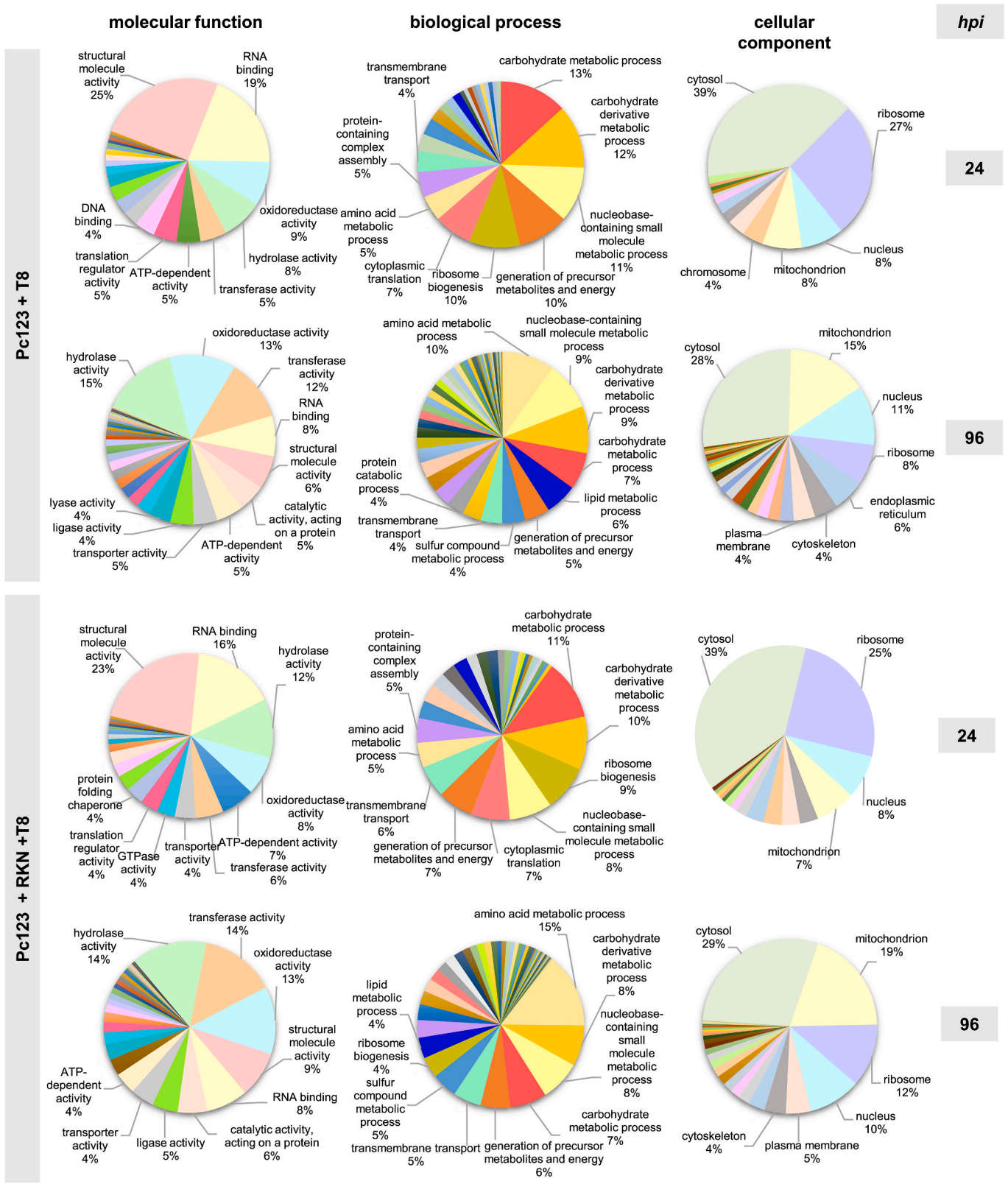


Fig. 8. Functional distribution and Gene Ontology (GO) annotation of the Pochonia chlamydosporia (Pc123) proteome under chitosan (T8) elicitation and nematode (RKN) interaction. The pie charts represent the functional landscape of Pc123 treated with chitosan, comparing the fungus in isolation (Pc123+T8) versus the tripartite interaction with *Meloidogyne javanica* eggs (Pc123+RKN + T8). Data are classified into Biological Process (BP), Molecular Function (MF), and Cellular Component (CC) categories. To highlight the most dominant metabolic and structural shifts induced by the elicitor, only GO terms accounting for ≥4% of the total relative proteome abundance are shown. This analysis reveals how chitosan modulates the fungal functional repertoire during the interaction with the host. Abbreviations: hpi, hours post-inoculation; RKN, *M. javanica*.

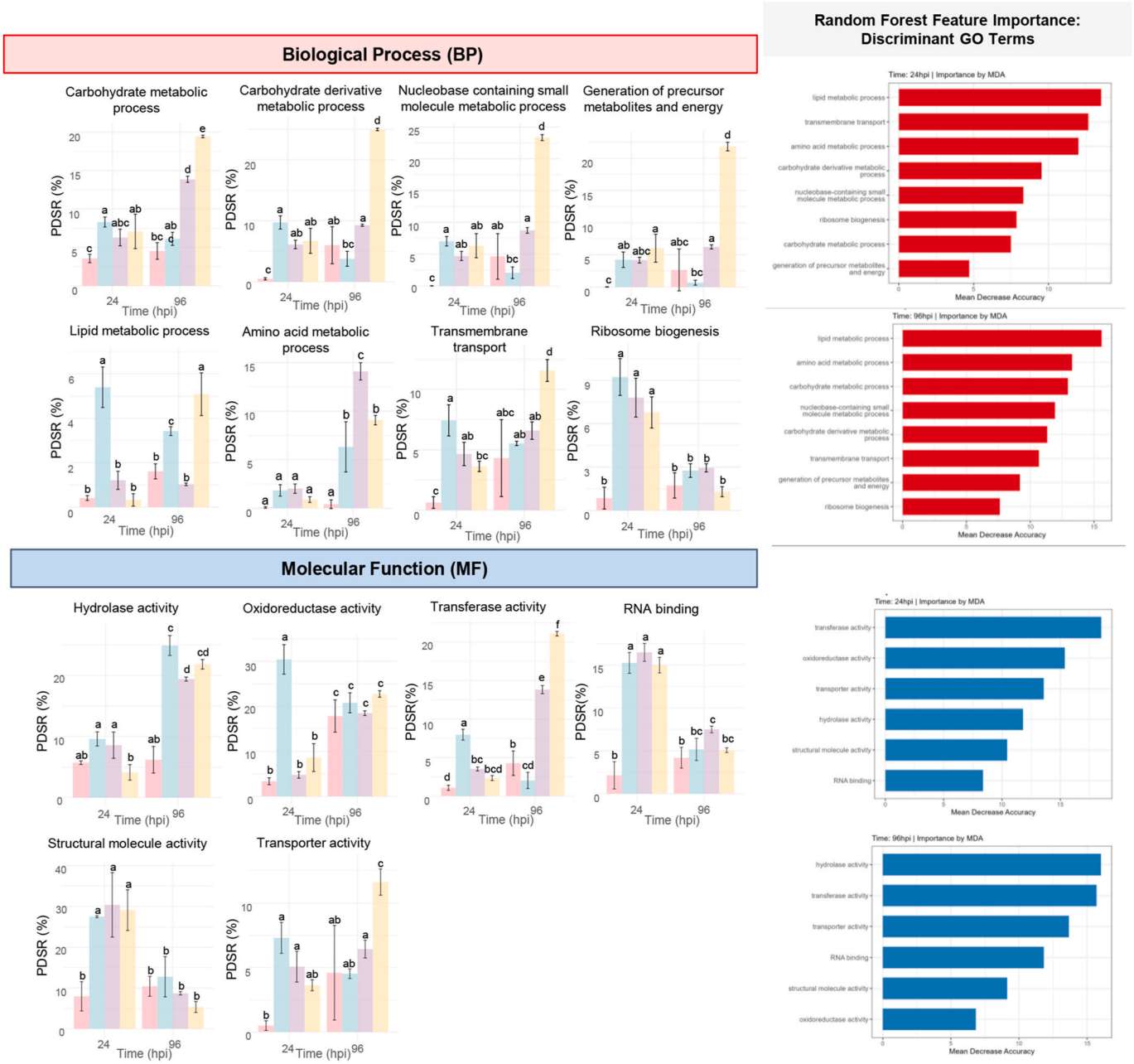


Fig. 9. Functional enrichment and discriminant analysis of the P. chlamydosporia proteome under chitosan and nematode stress. Left panels: Statistical validation of Gene Ontology (GO) terms across Biological Process (BP), Molecular Function (MF), and Cellular Component (CC) categories based on relative abundance (*PDSR*). Significant differences were identified by ANOVA followed by Tukey's HSD test ($p < 0.05$), with lowercase letters indicating distinct groups. At 24 hpi, **structural molecule activity** and **RNA binding** were the dominant functions, whereas at 96 hpi **hydrolase activity** and **amino acid metabolism** were most enriched, particularly in the PcRKNT8 treatment. Right panels: Random Forest (RF) feature-importance analysis (Mean Decrease Accuracy, MDA) for each GO category at 24 and 96 hpi. At 24 hpi, the MF model achieved **100% accuracy** (***OOB error*** = **0.00%**), with **lipid metabolic process** and **transmembrane transport** emerging as the most discriminant BP terms. By 96 hpi, discriminant features shifted toward degradative and energy-intensive pathways, with the **extracellular region** and **mitochondrion** becoming the top CC predictors, reflecting a transition to an externalized enzymatic and high-energy parasitic state enhanced by chitosan. Abbreviations: hpi, hours post-inoculation; *OOB*, out-of-bag error; *PDSR*, protein detection sampling rate; Pc, P. chlamydosporia; RKN, *M. javanica*; T8, chitosan.

transformation was applied.

The global PLS-DA explained **36.12%** of the variance in component 1 and **16.96%** in component 2. Repeated M-fold cross-validation (5 folds, 10 repetitions) yielded overall error rates between **0.51 and 0.87**. The 10 proteins with the highest absolute loadings in component 1 were extracted as the most discriminant variables.

2.10.3.4. Time-resolved PLS-DA and VIP biomarker identification (24 hpi and 96 hpi). Independent multiclass PLS-DA models were constructed for **24 hpi** and **96 hpi** to characterize temporal shifts in proteomic responses. For each time point, VIP scores were extracted from component 1, and the **top 30 proteins** with the highest VIP values were retained as discriminant biomarkers. Bubble-map visualizations were generated.

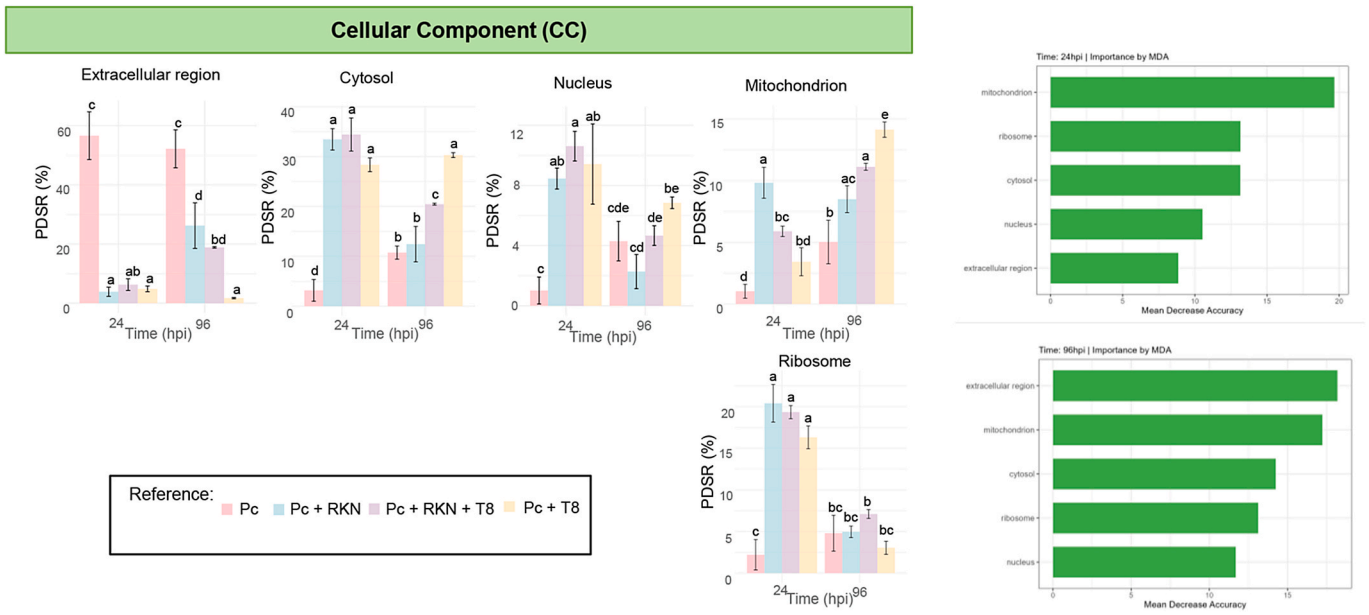


Fig. 9. (*continued*).

2.10.3.5. Comparative VIP heatmap (24 hpi, 96 hpi, global model). A VIP comparison matrix was constructed for the 60 proteins, incorporating VIP scores from the **24 hpi**, **96 hpi**, and **global** PLS-DA models. A Spectral-11 palette was used to visualize VIP magnitude across models, with markers highlighting proteins with **VIP ≥ 1.0** and **VIP ≥ 1.5**. Hierarchical clustering was applied to assess similarity among models.

2.10.3.6. Heatmap of the 60 combined VIP biomarkers. To compare abundance patterns across the **60 VIP biomarkers** (30 from 24 hpi and 30 from 96 hpi), a heatmap was constructed using **log-transformed PDSR values**. Missing values were replaced with zero.

A high-contrast heatmap was generated using a seven-colour multi-gradient palette, with hierarchical clustering applied to both rows and columns. Samples were automatically grouped into **24 hpi** and **96 hpi** clusters, and treatment-level annotations were included.

2.10.3.7. Random forest classification and biomarker importance. A **Random Forest (RF)** classifier was trained using the full Pc123 proteome following the ensemble methodology introduced by Breiman [41] and implemented through the *randomForest* package in R [42]. To ensure full reproducibility, a fixed random seed was applied prior to model training (**seed (123)**).

The model used **1500 trees**, with **34 variables sampled at each split**. The **out-of-bag (*OOB*) error rate was 20.83%**, and the confusion matrix showed perfect classification for most groups, with misclassification occurring primarily in PcRKNT8_24 and PcT8_24.

Protein importance was quantified using **Mean Decrease Accuracy**, and the **top 30 proteins** were retained as RF-derived biomarkers.

2.10.3.8. Random forest proximity-based MDS. To explore sample-level structure, an RF proximity matrix was computed by training a second model with proximity enabled. The proximity values were converted into a dissimilarity matrix (1 − proximity), and a **two-dimensional multidimensional scaling (MDS)** was performed. The MDS plot displayed the spatial distribution of samples according to RF-derived proximities, with points coloured by treatment and shaped by time point.

2.10.3.9. Heatmap of the top 30 random forest biomarkers. A heatmap was generated for the **top 30 RF biomarkers**, using log-transformed PDSR values and an 11-color Spectral palette scaled to quantiles of the data. Columns were annotated with treatment and time metadata, and hierarchical clustering was applied to both rows and columns.

2.10.3.10. Consensus biomarker identification between PLS-DA and random forest. To identify robust biomarkers consistently highlighted across machine-learning approaches, proteins were ranked by:

- **Mean Decrease Accuracy** (RF)
- **VIP_Global** (PLS-DA)

A combined ranking metric was computed as the average of the two ranks. The **eight proteins with the lowest average rank** were retained as the final consensus set. These proteins were used for downstream statistical modelling.

2.10.3.11. GLMM and tukey post-hoc tests for consensus biomarkers. To statistically evaluate abundance differences of the eight consensus proteins, **Generalized Linear Mixed Models (GLMMs)** were fitted using:

$$\log(PDSR) \sim \text{Condition} \times \text{Time} + (1|\text{Replicate})$$

Estimated marginal means (EMMs) were computed, and **Tukey-adjusted pairwise contrasts** were performed within each time point. All contrasts and p-values were compiled into a unified table for Supplementary Materials.

For each protein, EMMs with 95% confidence intervals and Tukey letter annotations were plotted to visualize treatment-specific differences.

2.10.3.12. GLMM diagnostics and post-hoc analysis for the lead RF biomarker. The **top-ranked RF biomarker** was analysed independently using the same GLMM framework. Model diagnostics were performed using DHARMa simulated residuals. Tukey-adjusted post-hoc comparisons were computed and visualized using EMM plots with confidence intervals and compact letter displays.

All multivariate and machine-learning analyses described in section 2.8.3 were conducted in R version 4.4.3 [43].

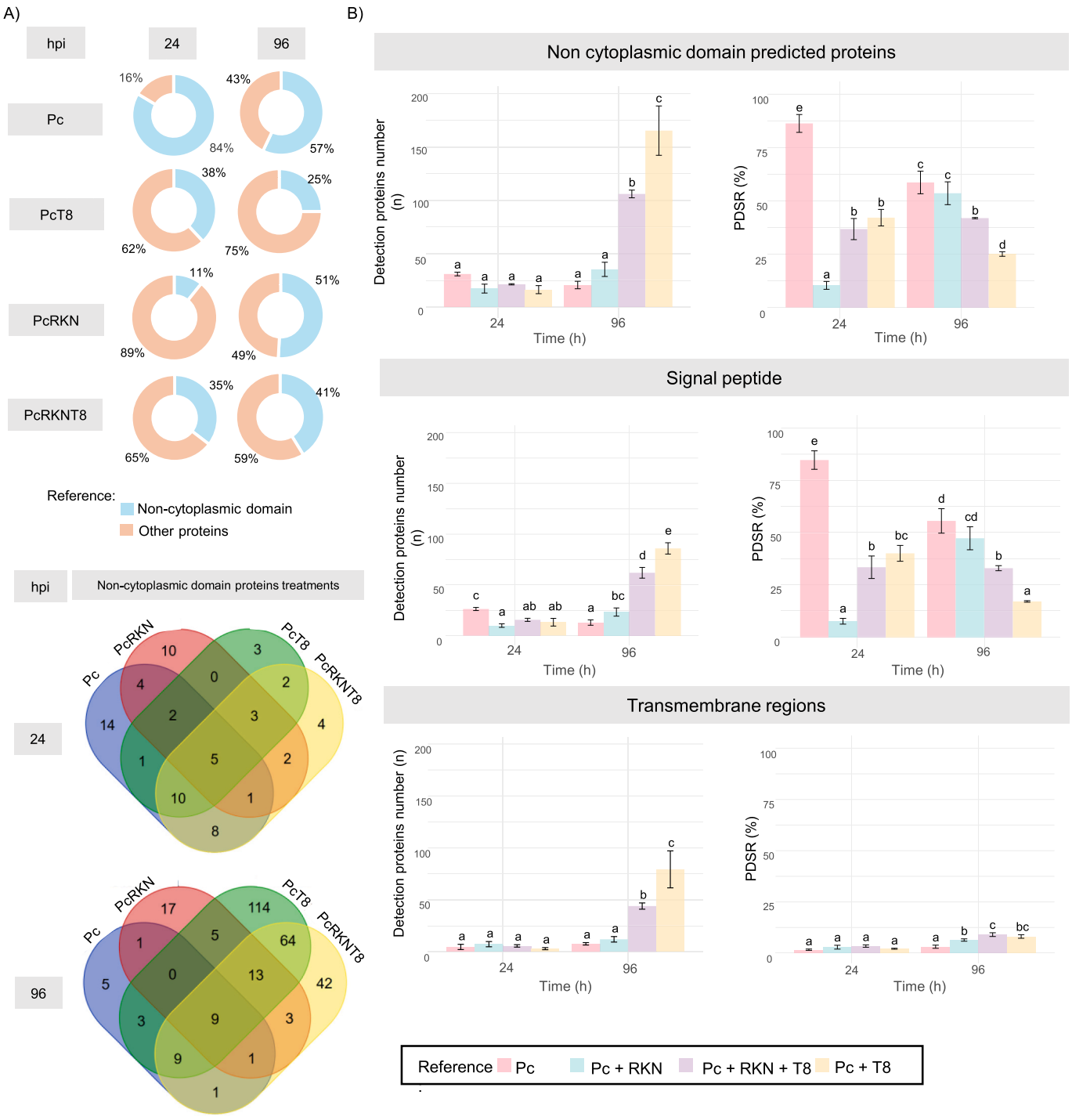


Fig. 10. Non-cytoplasmic domain proteins and secretory features of the P. chlamydosporia proteome under chitosan and nematode stress. (A) Cumulative average detection (*AD*, top) and distribution of protein counts (bottom) for each treatment at 24 and 96 hpi. Treatments with RKN and T8 showed early enrichment of proteins with non-cytoplasmic domains, with PcRKNT8 displaying the strongest increase at 96 hpi. (B) **Quantification of proteins containing non-cytoplasmic domains, signal peptides** (SP), and **transmembrane helices** (TM), together with their *nS* and *PDSR* values. Significant differences among treatments were determined using ANOVA followed by Tukey's HSD test (< 0.05), indicated by lowercase letters. Abbreviations: *AD*, average detection; hpi, hours post-inoculation; *nS*, total number of proteins detected in a single sample; *PDSR*, protein detection sampling rate; SP, signal peptide; TM, transmembrane region; Pc, *Pochonia chlamydosporia* strain 123; RKN, *M. javanica* eggs; T8, chitosan.

2.10.4. Functional profiling of Pc123 and M. javanica: GO-term statistics and random forest classification

Gene Ontology (GO) term abundance profiles derived from *PDSR* values were used to characterize functional changes in Pc123 and *Meloidogyne javanica* across treatments and time points (S.13). For each GO term, a two-factor **ANOVA** (*treatment* × *time*) was performed, followed by **Tukey's HSD** post-hoc tests when significant effects were detected. Model assumptions were evaluated using the **Shapiro–Wilk test** for residual normality and **Levene's test** for variance homogeneity. All statistical analyses were conducted in R version 4.3.3 [40].

To complement the linear modelling framework and identify the most discriminant functional signatures, **six RF models** were trained for



Fig. 11. Sequence–feature space and functional clustering of non-cytoplasmic proteins in P. chlamydosporia under chitosan and nematode stress. Central panel: Principal Coordinates Analysis (PCoA) of proteins containing non-cytoplasmic features (full-sequence, Non-Cyt sequence, signal peptides, SP; transmembrane helices, TM) across treatments at 24 and 96 hpi. Clusters represent groups of proteins with similar sequence-derived structural features. Left panels (24 hpi) and right panels (96 hpi): For each cluster, the percentage of proteins containing SP and TM regions is shown together with the three most enriched Gene Ontology (GO) terms. Percentages of SP and TM do not sum to 100% because these features are not mutually exclusive; many fungal proteins possess both a signal peptide and one or more transmembrane helices, particularly secreted or membrane-anchored enzymes involved in parasitism and stress responses. BP GO-ID: GO:0005975, carbohydrate metabolic process; GO:1901135, carbohydrate derivative metabolic process; GO:0055085, transmembrane transport.CC GO-ID: GO:0005576, extracellular region; GO:0005618, cell wall; GO:0005783, endoplasmic reticulum; GO:0005886, plasma membrane; GO:0005739, mitochondrion; GO:0005829, cytosol. MF GO-ID: GO:0016787, hydrolase activity; GO:0016491, oxidoreductase activity; GO:0005215, transporter activity; GO:0140657, ATP-dependent activity; GO:0003924, GTPase activity. Abbreviations: Pc, *Pochonia chlamydosporia* strain 123; RKN, *Meloidogyne javanica* eggs; T8, chitosan.

each proteome—one for each combination of **GO category** (Biological Process, BP; Molecular Function, MF; Cellular Component, CC) and **time point** (24 hpi, 96 hpi). Prior to training, a fixed random **seed (123)** was applied to ensure reproducibility. All RF analyses were performed in R version 4.4.3 [43]. Each model used **1000 trees**, and performance was evaluated using the **out-of-bag (*OOB*) error rate** and corresponding **classification accuracy**.

2.10.4.1. Random forest classification performance for Pc123. Pc123 exhibited **moderate functional separability at 24 hpi** and **strong discriminability at 96 hpi**, particularly in MF and BP categories(see Table 1).

These results indicate that **Pc123 functional profiles become increasingly distinct across treatments over time**, with MF terms showing exceptional discriminative power at 24 hpi and all categories achieving high accuracy at 96 hpi.

2.10.4.2. Random forest performance summary for M. javanica. *M. javanica* showed **limited functional separability at 24 hpi**, especially in MF, but displayed **strong divergence at 96 hpi**, particularly in BP and MF categories(see Table 2).

The poor MF performance at 24 hpi suggests **substantial functional overlap** between MELJA_Pc and MELJA_Pc_T8 early in infection. By contrast, the perfect BP classification at 96 hpi indicates **strong functional divergence** in biological processes during later infection stages.

2.10.4.3. Integrated interpretation. Across both organisms:

- **Pc123** shows **earlier and stronger functional differentiation**, particularly in MF at 24 hpi and across all categories at 96 hpi.
- **MELJA** displays **delayed functional divergence**, with weak separability at 24 hpi but strong BP and MF discrimination at 96 hpi.
- **MF terms** tend to be the most discriminant overall, especially early in Pc123 and late in MELJA.
- **CC terms** show moderate discriminability in both proteomes, with less pronounced temporal shifts.

Together, the ANOVA-based statistical framework and the category-specific RF models provide a comprehensive view of functional reprogramming in Pc123 and *M. javanica*, revealing organism-specific temporal patterns in GO-term differentiation.



Fig. 11. (*continued*).

2.10.5. Sequence Feature-space, phylogenetic comparison, and localization-driven signals in non-cytoplasmic domains

In addition to the domain-based classification (2.9), the amino acid sequences of all non-cytoplasmic (Non-Cyt) proteins were utilized to construct a sequence-based feature space (**Amino Acid Feature Vectorization**, 2.10.5.1). This approach enabled the comparison of sequence-derived properties against two complementary phylogenetic frameworks:

1. **Evolutionary Phylogeny**, based on full-length peptide sequences.
2. **Localization-based Phylogeny**, specifically focused on non-cytoplasmic domain sequences.

This methodological framework (Fig. 1E2) was executed through an integrated analytical pipeline combining **amino acid feature space modelling** (2.10.5.1), **unsupervised clustering** (2.10.5.2), **multivariate ordination** (2.10.5.3), **phylogenetic reconstruction** (2.10.5.4), and **Mantel correlation tests** (2.10.5.5-6). Finally, **machine learning-driven functional analyses** (2.10.5.7-11) were implemented across all experimental scenarios (treatment × time).

2.10.5.1. Amino-acid feature vectorization of protein domains. Each protein was decomposed into four sequence components: full peptide sequence, Non-Cyt domain, signal peptide (SP), and transmembrane (TM) region (S.14). A robust vectorization pipeline extracted 20-dimensional amino-acid composition vectors for each domain using the *Peptides* package. All sequences were sanitized to remove non-alphabetic characters, ensuring reproducibility across annotation formats.

The resulting **80-feature matrix** (20 AA frequencies × 4 domains + sequence length) was filtered to remove zero-variance columns, preventing singularities in ordination and clustering.

2.10.5.2. Optimal clustering of the feature space. Silhouette-based cluster optimization ($k = 2 - 8$) was performed using k-means clustering to quantify intrinsic structure in the 80-feature matrix. This analysis assessed whether proteins naturally grouped according to their structural domain composition. When the number of unique feature vectors was insufficient for robust clustering, the analysis defaulted to phylogenetic validation.

2.10.5.3. PCoA visualization of structural feature space. Euclidean distances were computed (after scaling and numerical stabilization via jittering), followed by **Principal Coordinates Analysis (PCoA)** using classical multidimensional scaling (*cmdscale*, $k = 2$).

For each scenario, the first two PCoA axes were plotted, with points coloured by structural cluster and labelled by UniProt ID. These ordinations provided an interpretable, low-dimensional representation of structural variation and allowed direct comparison with phylogenetic and localization-driven signals.

2.10.5.4. Phylogenetic reconstruction of non-cyt and full sequences. Phylogenies were reconstructed for both Non-Cyt domain sequences and full peptide sequences. Sequences were aligned using ClustalW (*msa*), converted to amino-acid *phyDat* objects, and used to compute maximum-likelihood distance matrices (*phangorn*). Neighbor-joining trees were generated, and tip labels were mapped to structural clusters. Tree fidelity was evaluated using cophenetic correlation between tree-derived distances and structural feature-space distances.

2.10.5.5. Mantel tests: linking structure, localization, and evolution. To quantify the relationship between structural feature-space distances, Non-Cyt phylogenetic distances, and full-sequence phylogenetic distances, **Mantel tests** (Spearman, 999 permutations) were performed for each scenario.

2.10.5.6. Comparative mantel results across all scenarios (see Table 3).

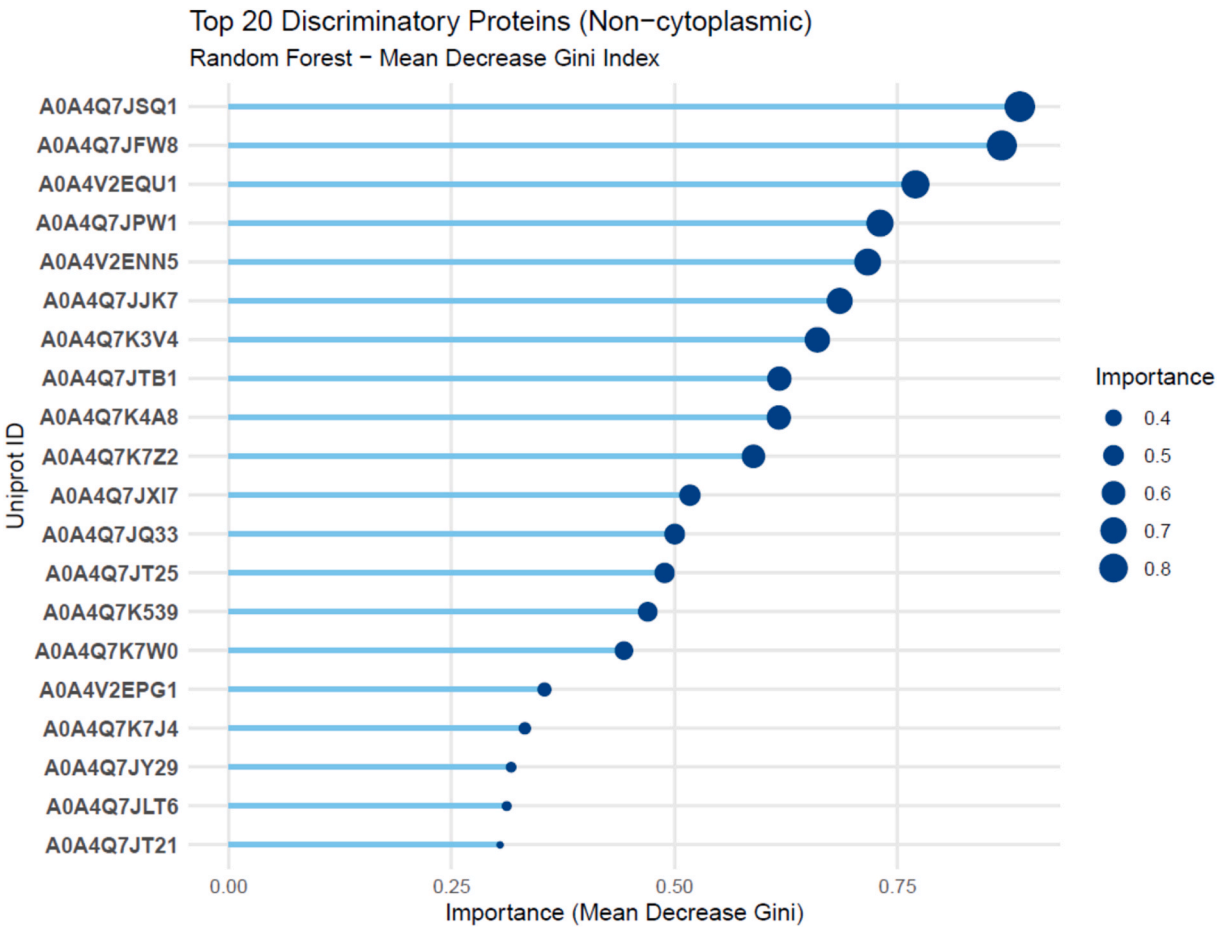


Fig. 12. Random Forest (RF) prioritization of non-cytoplasmic drivers for Cellular Component (CC) prediction. Top 20 discriminatory proteins identified by a **RF** classifier (2000 trees, *mtry* = 5) based on the Mean Decrease Gini Index. The model identifies key structural and enzymatic features that drive the differentiation of *P. chlamydosporia* 123 across experimental conditions and define its spatial proteomic organization. The leading drivers include energy-related transporters (**ATP synthase subunit alpha**, A0A4Q7JSQ1; **ADP/ATP translocase**, A0A4Q7JFW8), structural components (**CWP1–3**, A0A4V2EQU1, A0A4Q7K539, A0A4Q7JPW1), and specialized hydrolases associated with host-wall degradation (**Glucoamylase**, A0A4Q7K7Z2; **GH18 chitinase**, A0A4Q7JT25; **β-glucosidase**, A0A4Q7JLT6). To validate the influence of treatment and time on these biomarkers, individual GLMMs and Tukey's HSD post-hoc tests ($p < 0.05$) were conducted for each protein, results and significance levels are detailed in **Supplementary Data S.15.** While the global ***OOB*** error rate was 50%, these 20 proteins represent the most stable features for class discrimination within the non-cytoplasmic proteome. Abbreviations: CWP: Cell Wall Protein; GH18: Glycosyl Hydrolase family 18 (Chitinases); GLMM: Generalized Linear Mixed Model; *OOB*: Out-of-Bag (error rate).

2.10.5.6.1. Interpretation.

- **Localization (Non-Cyt) dominates** in most scenarios, especially at 96 hpi.
- **Evolutionary signal (full sequence)** dominates only in PcT8_24, PcRKNT8_24, and significantly in PcRKNT8_96.
- The **only significant correlation** (PcRKNT8_96) indicates that under combined RKN + T8 stress at 96 hpi, **global evolutionary divergence** better explains structural variation.
- Cophenetic correlations were generally low, reinforcing the need for combined structural–phylogenetic approaches.

2.10.5.7. Machine-learning analysis of non-cyt proteins using GO.db (global CC-driven model). To complement the OmicsBox-based CC analysis, we performed a **machine-learning analysis** (S.15) using the complete GO.db ontology to identify all proteins annotated to the **Cellular Component (CC)** namespace.

2.10.5.8. Extraction of CC-annotated proteins (GO.db). All GO terms belonging to the CC ontology were retrieved from GO.db, and proteins annotated with these terms were extracted and cross-referenced with PDSR abundance profiles to build a unified machine-learning-dataset.

2.10.5.9. Random forest classification across all conditions and time points. A RF classifier (OBB: 50%, 2000 trees, seed (123)) was trained using:

- **Predictors:** *PDSR* abundance of all CC-annotated Non-Cyt proteins
- **Response:** Combined condition × time group (e.g., Pc_24, PcRKN_96)

Missing values were imputed using **minimum(*PDSR*)/10**, ensuring model stability without biasing abundance distributions.

The model identified the **Top 20 most discriminant non-cyt proteins** across all experimental conditions.

A high-resolution **lollipop plot** was generated to display the Mean Decrease Gini importance of the Top 20 proteins, providing a clean and interpretable ranking of discriminant features.

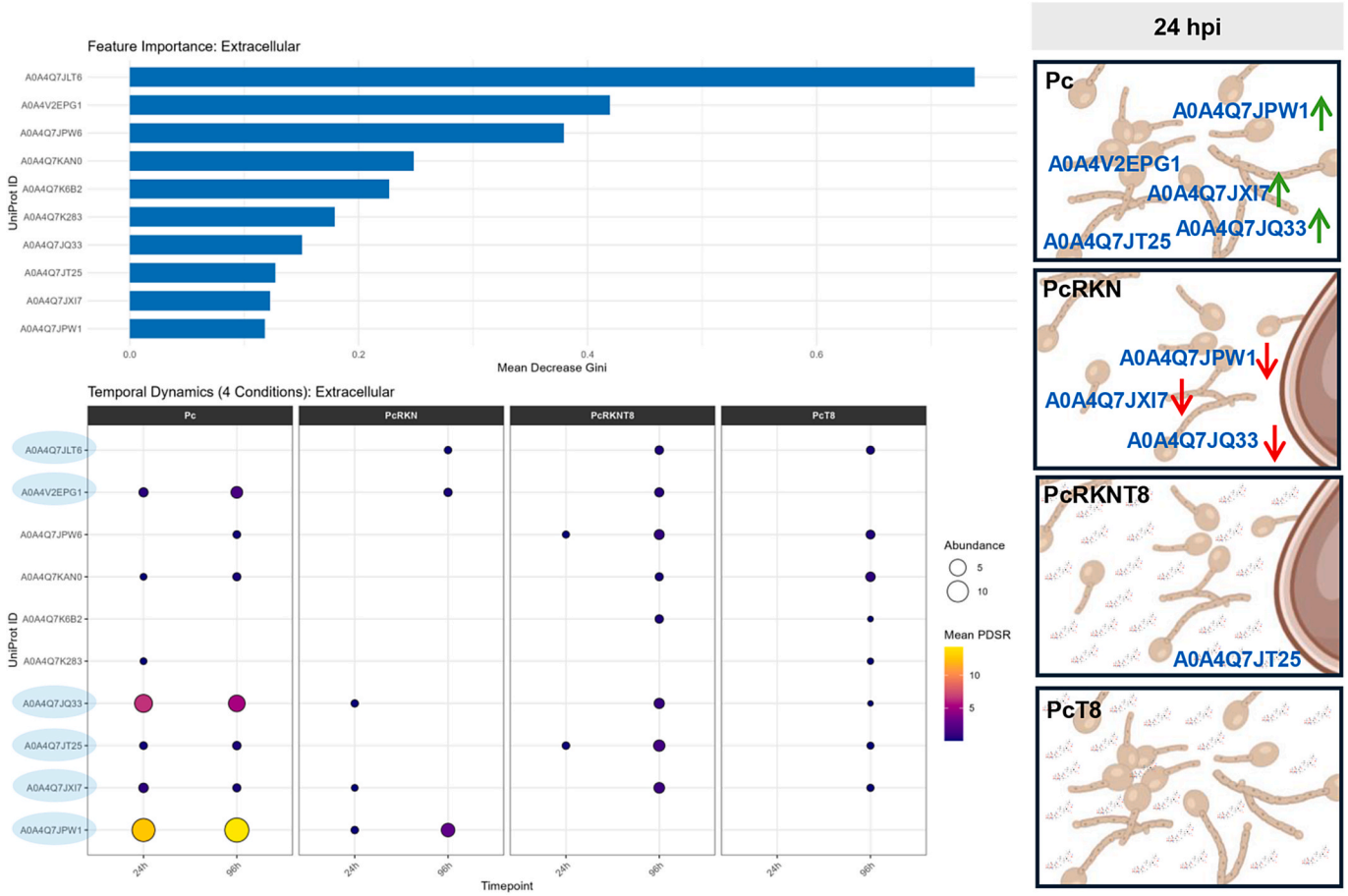


Fig. 13. Spatial prioritization of the Pc123 secretome: Extracellular and Membrane compartments. This figure integrates machine learning prioritization (RF), relative abundance (bubble plots), and biological context (cartoons) to resolve the spatial organization of the non-cytoplasmic proteome.

- **Top-left panel:** RF top 10 predictors for the **Extracellular** category, led by **Glucan 1,3-β-glucosidase** (A0A4Q7JLT6). The bubble plot displays the mean ***PDSR*** across experimental conditions (Pc, PcRKN, PcRKNT8, and PcT8).
- **Bottom-left panel:** RF top 10 predictors for the **Membrane** category, led by **Cupin-type protein** (A0A4Q7K1K2).
- **Right panel:** Schematic cartoons representing fungal–host interactions and secretory deployment for each condition.
- **Visual Coding and Symbology:**
  - **Blue circles/text:** Top 20-RF drivers (identified in Fig. 12). Six leading extracellular proteins—Glucan 1,3–glucosidase (A0A4Q7JLT6), CFEM domain-containing protein 1 (A0A4V2EPG1), Heterokaryon incompatibility protein (A0A4Q7JQ33), GH18 chitinase (A0A4Q7JT25), Glycosidase 1 (A0A4Q7JXI7), and Cell wall protein 3 (A0A4Q7JPW1)—are highlighted.
  - **Green circles/text:** Relevant functional biomarkers identified by high abundance (mean PDSR) in the Membrane fraction, specifically **Cupin-type protein** (A0A4Q7K1K2), **Putative adhesin** (A0A4Q7K4R2), and **Copper acquisition factor BIM1-like** (A0A4Q7KA57).
  - **Directional arrows/schematic cartoons:** Red arrows indicate up/down-abundance relative to Pc (control); green arrows vs. **PcRKN**; and blue arrows vs. **PcT8**.
  - **Statistical validation/:** The arrow colours denote significant pairwise differences ($p < 0.05$) based on **GLMM** followed by **Tukey's HSD post-hoc** tests

Schematic illustrations were created using **BioRender.com**. The chemical structure of chitosan was modelled based on **Chitosan from shrimp shells (PubChem CID 71853). Abbreviations: GLMM**, Generalized Linear Mixed Model; **RF**: Random Forest; **Tukey's HSD**: Tukey's Honestly Significant Difference test.

2.10.5.10. Statistical Validation via GLMM + tukey. To validate the machine-learning-derived proteins statistically, a **Gamma GLMM** (log link) was fitted for each protein:

$$\mathrm{PDSR}_{adj} \sim \mathrm{Group} + (1|\mathrm{Replicate})$$

Estimated marginal means were computed and Tukey-adjusted pairwise contrasts were extracted for all significant comparisons ($p < 0.05$).

2.10.5.11. Cellular-component (GO-CC) analysis of non-cyt domains (OmicsBox). GO-term annotations from OmicsBox were mapped to four major cellular-component (CC) groups: **Extracellular**, **Membrane**, **Cytoplasmic**, and **Intracellular/Organelle**. Presence/absence matrices were constructed for each group across conditions and time points.

RF models (1000 trees, seed (123)) were trained to discriminate **24 hpi vs. 96 hpi** within each CC group. Top 10 discriminant proteins were extracted and visualized using:

- **Feature-importance barplots** (Gini index)
- **Temporal bubble plots** (mean *PDSR* across conditions × time)

These analyses revealed strong temporal differentiation in extracellular and membrane proteins, while cytoplasmic and organelle-associated proteins showed more stable profiles.

All analyses related to non-cytoplasmic domain characterization—including

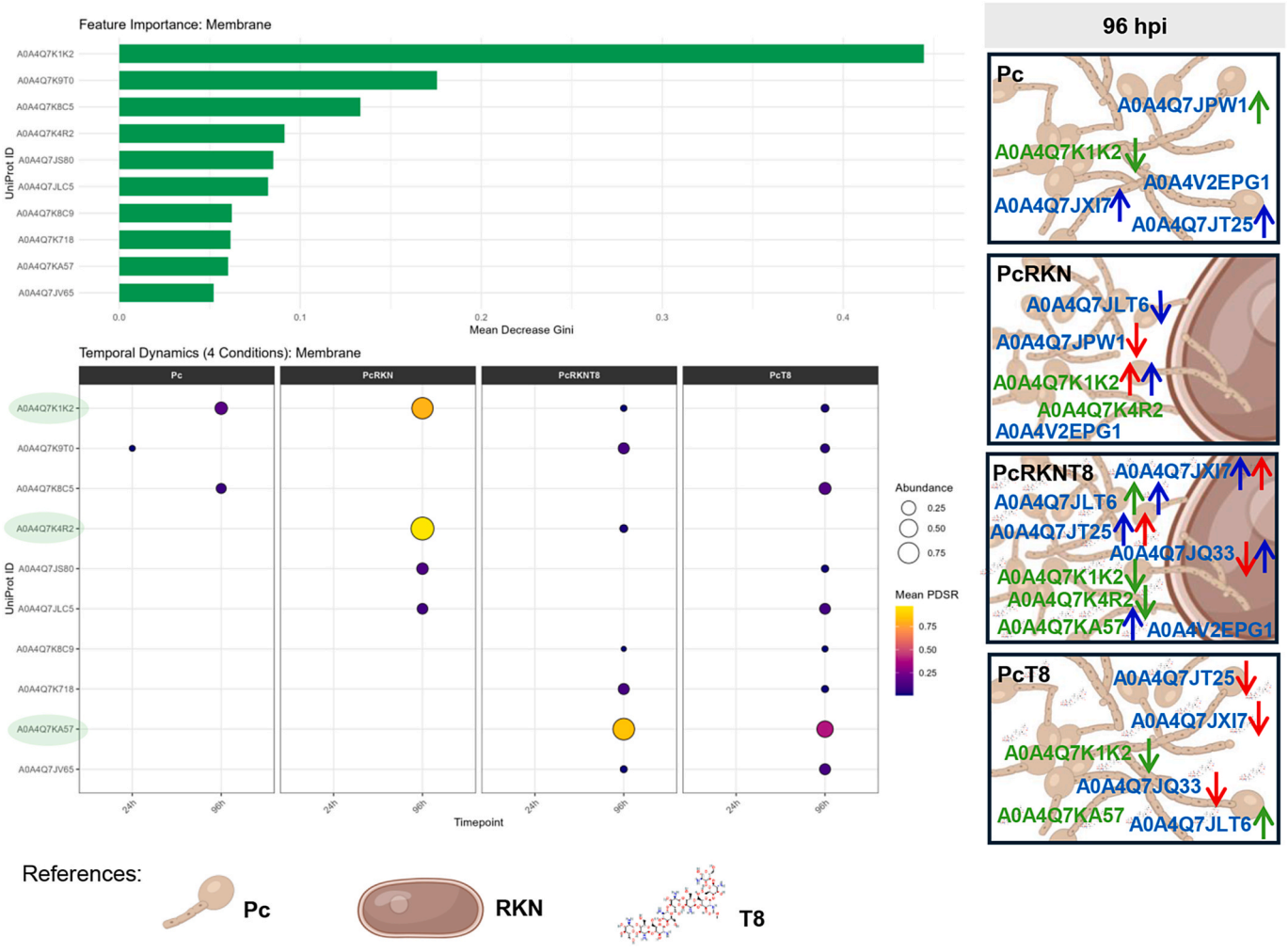


Fig. 13. (*continued*).

sequence-feature extraction, structural clustering, phylogenetic reconstruction, and Mantel comparisons—were performed using R v4.4.3 [43].

2.10.6. Integrated proteomic and machine-learning analysis of Meloidogyne javanica eggs under chitosan treatment

The proteomic response of *Meloidogyne javanica* (MELJA) eggs during parasitism was analysed to determine how chitosan (T8) affects the nematode at early (24 hpi) and late (96 hpi) infection stages. Unlike the fungal system (Pc123), where biomass increases over time, the **egg concentration remains constant** (10 RKN eggs × 280 *drops* = 2,800 *RKN eggs* per sample), meaning that the MELJA dataset reflects a **static developmental stage exposed to dynamic host-derived pressures**. This makes the system ideal for evaluating the direct impact of chitosan on parasitic viability and early infection processes (Fig. 1E3; S.16).

2.10.6.1. Differential abundance and volcano plot analysis. Protein abundance profiles (*PDSR*) were compared between MELJA_Pc and MELJA_Pc_T8 at each time point. $\log_2$FC revealed clear treatment-dependent shifts, visualized through high-resolution Volcano plots. These analyses showed:

- **early suppression of metabolic and enzymatic proteins** at 24 hpi,
- **late activation of stress-response and structural proteins** at 96 hpi,
- a progressive remodelling of the parasitic proteome under chitosan exposure.

2.10.6.2. Machine-learning framework for MELJA proteomic discrimination. To characterize the MELJA proteome under chitosan treatment, we implemented a multi-algorithm machine-learning pipeline combining **Random Forest, PLS-DA**, **SVM**, and **consensus analysis**.

2.10.6.3. Random forest classification. A RF classifier (2000 trees, seed (123)) identified the top 30 proteins with the highest Mean Decrease Gini importance. These proteins represent the strongest statistical drivers of treatment discrimination. **The model was trained using the full MELJA proteome matrix, excluding replicate identifiers, and the Group factor was used as the response variable.**

To evaluate model robustness and the internal structure of the dataset, we examined the **Out-of-Bag (*OOB*) error**, which provides an unbiased estimate of classification performance. The final model yielded an ***OOB* of 41.67%**, indicating moderate class overlap consistent with the biological variability observed in the nematode proteome.

The RF confusion matrix showed that samples from MELJA_Pc_96 were classified with perfect accuracy (class.error = 0), whereas MELJA_Pc_24 and MELJA_Pc_T8_24 exhibited higher misclassification rates (class.error = 0.67). MELJA_Pc_T8_96 showed intermediate

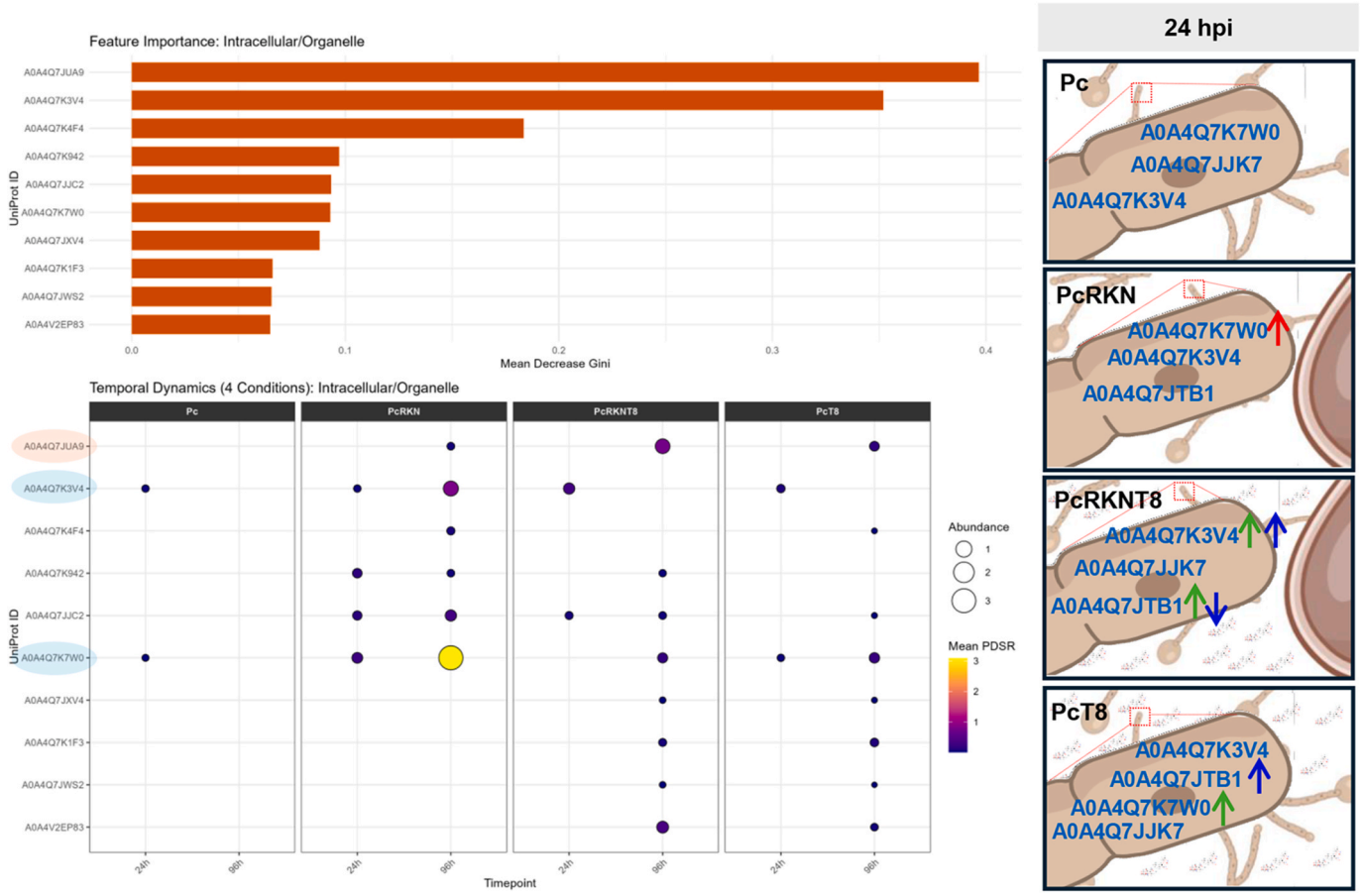


Fig. 14. Spatial prioritization of non-cytoplasmic Pc123 proteome: Intracellular/Organelle and Cytoplasmic compartments. Following the architecture of Fig. 15, this panel resolves the internal cellular drivers of the Pc123 response under stress.

- **Top-left panel:** RF top 10 predictors for **Intracellular/Organelle** features, led by **Methylmalonate-semialdehyde dehydrogenase** (A0A4Q7JUA9).
- **Bottom-left panel:** RF top 10 predictors for **Cytoplasmic** features, led by **Formate dehydrogenase** (A0A4Q7JTB1).
- **Right panel:** Schematic cartoons detailing the internal metabolic restructuring and enzymatic mobilization during the transition from a saprotrophic to a parasitic state
- **Visual Coding and Symbology:**
  - **Blue circles/text:** Top 20-RF drivers (Fig.12). In the Intracellular/Organelle group, these include **α-1,2-Mannosidase** (A0A4Q7K3V4) and **AB hydrolase-1** (A0A4Q7K7W0). In the **Cytoplasmic** group, only two proteins from the global top 20 RF are highlighted: **Formate dehydrogenase** (A0A4Q7JTB1) and **Catalase** (A0A4Q7JJK7).
  - **Orange circles/text (Intracellular/Organelle):** Relevant functional biomarkers identified by abundance, such as the top-ranked **Methylmalonate-semialdehyde dehydrogenase** (A0A4Q7JUA9).
  - **Directional arrows/schematic cartoons:** Indicate abundance shifts relative to **Pc** (red), **PcRKN** (green), and **PcT8** (blue).
  - **Statistical validation/schematic cartoons:** Arrows denote significant comparisons ($p < 0.05$) derived from individual **GLMM/Tukey** diagnostics for each protein.

Schematic illustrations were created using **BioRender.com**. The chemical structure of chitosan was modelled based on **Chitosan from shrimp shells (PubChem CID 71853). Abbreviations: GLMM**, Generalized Linear Mixed Model; **RF**: Random Forest; **Tukey's HSD**: Tukey's Honestly Significant Difference test.

performance (class.error = 0.33). **These patterns confirm that the proteomic profiles of each condition are distinguishable, but also reflect the intrinsic variability of the nematode response, particularly at early infection stages.**

2.10.6.4. PLS-DA (partial least squares discriminant analysis). PLS-DA was performed separately for 24 hpi and 96 hpi. The top 30 proteins per time point were extracted based on VIP scores.

PLS-DA revealed:

- strong separation between treatments at both time points,
- distinct discriminant proteins at 24 vs. 96 hpi,
- increased model stability at 96 hpi (higher Q^2, lower BER).

Permutation tests and AUC metrics confirmed the robustness of the models.

2.10.6.5. Support vector machine (SVM). An SVM with a linear kernel identified proteins contributing most strongly to the separating hyperplane between MELJA_Pc and MELJA_Pc_T8. The **top 30 SVM drivers** were extracted based on squared weight magnitudes.

2.10.6.6. Consensus analysis across machine-learning-methods. To address biological variability and cluster dispersion, a consensus-based approach was implemented. Three sets were compared:

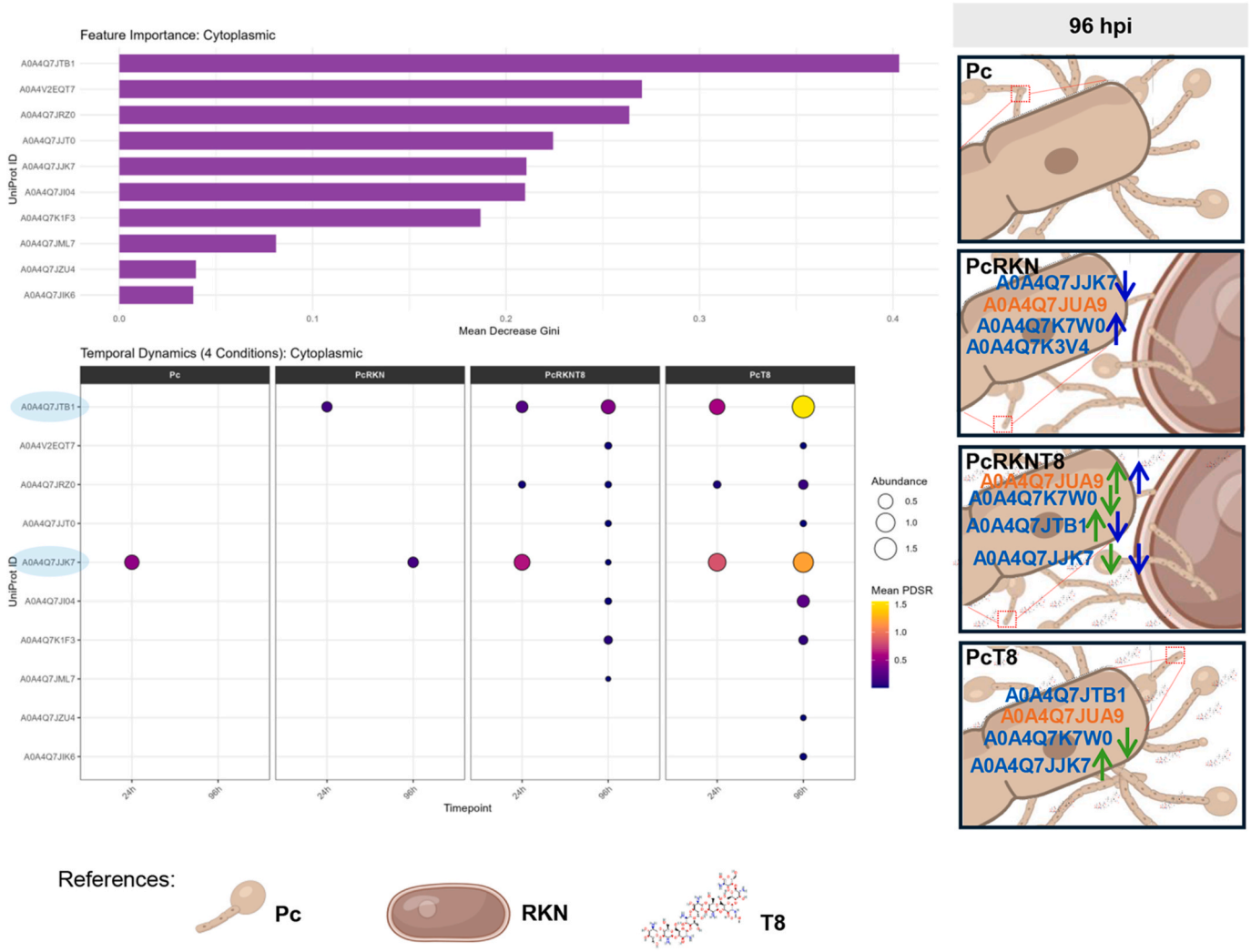


Fig. 14. (*continued*).

- Top 30 RF proteins
- Top 30 SVM proteins
- Top 30 PLS-DA proteins (24 hpi + 96 hpi)

A Venn diagram identified:

- **13 strict consensus proteins** (RF ∩ SVM ∩ PLS-DA)
- **a broader flexible consensus** (present in ≥2 methods)

The 13 strict consensus proteins represent the **core chitosan-responsive parasitic signature** of *M. javanica* eggs.

2.10.6.7. Statistical Validation and Kinetic Profiling of consensus biomarkers. Each of the 13 consensus proteins was validated using a hierarchical statistical approach. A Gamma GLMM with log link was fitted whenever possible:

$$PDSR_{adj} \sim \text{Condition} \times \text{Time} + (1|\text{Replicate})$$

When the Gamma model failed, a log-linear model was used. Estimated marginal means and Sidak-adjusted pairwise contrasts ($p < 0.05$) were computed.

Two complementary visualizations were generated for each protein:

- **Condition-specific comparisons at each time point**, with estimated means and Sidak significance letters.
- **Kinetic trend plots**, showing replicate dispersion, mean trajectories, and confidence intervals across 24 and 96 hpi.

These analyses revealed coherent, time-dependent abundance patterns, with most proteins showing:

- **early suppression under chitosan at 24 hpi**,
- **partial recovery or compensatory overexpression at 96 hpi.**

2.10.6.8. Kinetic validation of the two RF-specific drivers. Two proteins (A0A915MDA7 and A0A915LIP9) were uniquely highlighted by RF. Condition × Time models and Sidak contrasts confirmed:

- strong treatment-specific shifts,
- clear kinetic divergence between MELJA_Pc and MELJA_Pc_T8,
- consistent replicate-level patterns.

These RF-exclusive proteins are therefore **high-confidence biomarkers** of chitosan-induced parasitic disruption.

2.10.6.9. Cellular-component (GO-CC) functional architecture of the MELJA proteome. GO-CC annotations were grouped into four macro-categories:

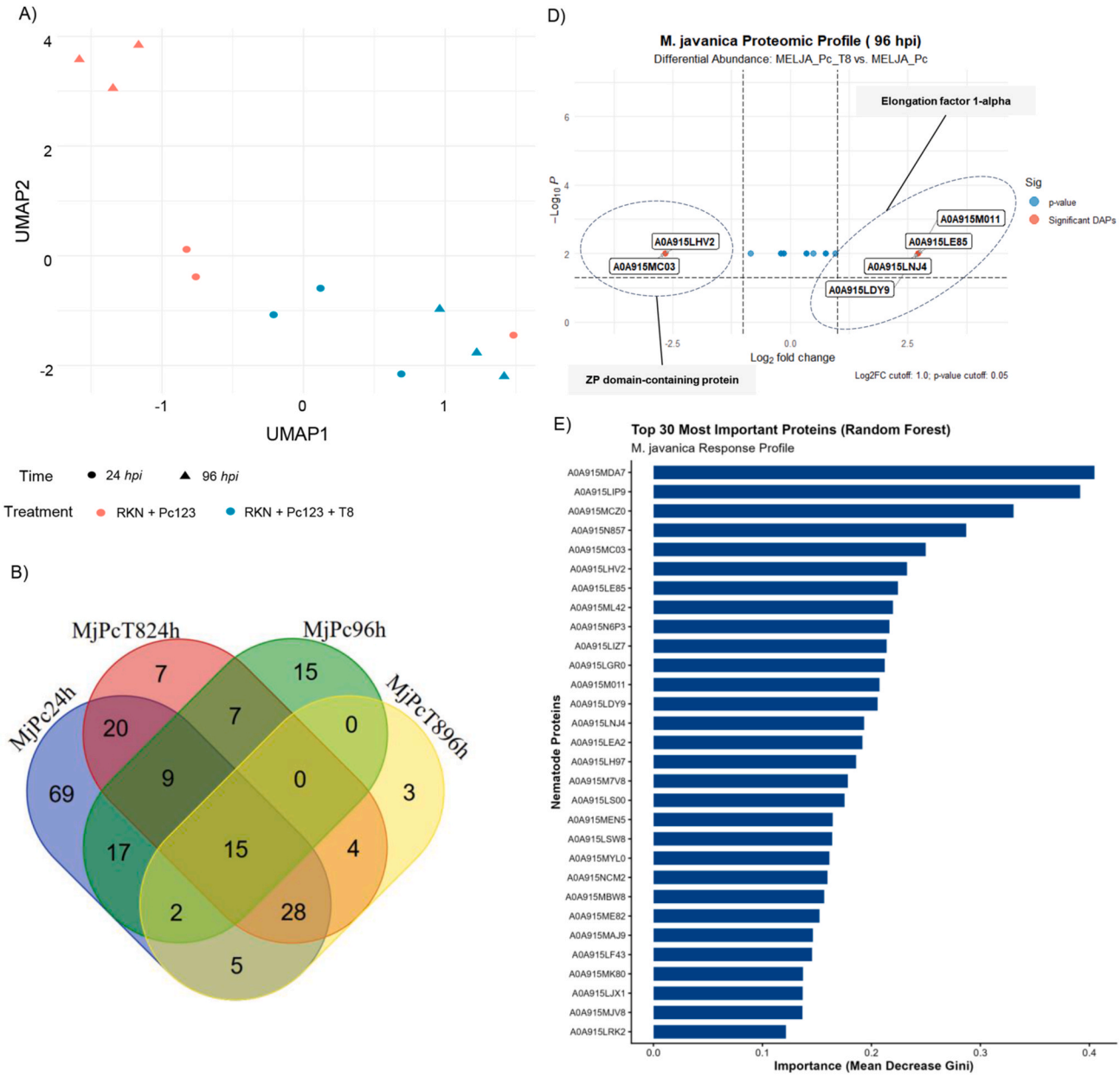


Fig. 15. Multi-omic characterization of the Meloidogyne javanica (MELJA) proteome during Pochonia chlamydosporia parasitism. The figure illustrates the dynamic modulation of the nematode proteome in response to fungal infection and chitosan (T8) elicitation. (A) UMAP Projection: Visualization based on protein presence/absence across samples. The separation of clusters confirms significant proteomic shifts driven by both time (24 vs. 96 hpi) and treatment (PERMANOVA, $R2 = 0.184$, $p = 0.011$). Comparative analysis of protein overlap. At 24 hpi, a 56.64% similarity was observed between treatments, whereas by 96 hpi, similarity dropped to 19.33%, indicating that chitosan significantly diversifies the nematode's proteomic response during late-stage parasitism. **(B) Venn Diagram:** Comparative analysis of the shared and condition-specific protein inventories across treatments and time points. The intersection reveals a core proteome of **15 proteins** consistently present in all conditions. At 24 hpi, a common core of **20 proteins** is shared exclusively between **MjPc** and **MjPcT8**, while the late stage (96 hpi) shows a convergence of **28 proteins** shared between both treatments. The diagram highlights a higher number of unique proteins in the parasitism control group (**69** at 24 hpi) compared to the chitosan-treated group (**7** at 24 hpi), reflecting the selective modulation of the nematode's protein profile. **(C) Differential Abundance at 24 hpi:** Volcano plot highlighting proteomic stability. Only **Vitellogenin domain-containing protein (A0A915MDA7)** showed significant up-regulation ($\log 2FC \approx 1.5$, $p \approx 0.01$), marking it as an early biomarker of the chitosan-induced response. **(D) Differential Abundance at 96 hpi:** Volcano plot identifying six Differential Abundant Proteins (DAPs). Up-regulated biomarkers include four isoforms of **Elongation factor 1-alpha (EF 1-α; A0A915M011, A0A915LDY9, A0A915LNJ4, A0A915LE85)** with a magnitude of $\log 2\,FC \approx 2.7$ (>6-fold increase). Down-regulated proteins include **ZP domain-containing protein (A0A915MC03and A0A915LHV2;** $\log 2\,FC \approx -2.7$). **(E) Global Random Forest (RF) Prioritization:** Top 30 discriminatory proteins ranked by Mean Decrease Gini Index. The model identifies **Vitellogenin domain-containing proteins (A0A915LIP9 and A0A915MDA7)** as the most influential features for classifying the nematode's physiological state. **(F) Kinetic Profiles of Leading Biomarkers:** Abundance trends (*PDSR*) for the top 2 RF proteins. **Vitellogenin domain-containing proteins (A0A915LIP9 and A0A915MDA7)** show high detection levels at 24 hpi ($AD = 4$– 6% in T8, Figure S.2E), followed by a significant abundance collapse by 96 hpi. Letters (a, b) denote statistical significance derived from **GLMM** followed by **Tukey's HSD post-hoc** tests ($p < 0.05$). Abbreviations: *AD*, Average Detection; GLMM, Generalized Linear Mixed Model; MjPc: Meloidogyne javanica parasitized by Pochonia chlamydosporia (parasitism control); MjPcT8: *M. javanica* parasitized by P. chlamydosporia in the presence of chitosan (T8); *PDSR*, Protein Detection Sampling Rate; PERMANOVA, Permutational Multivariate Analysis of Variance; UMAP, Uniform Manifold Approximation and Projection; Tukey'c HSD, Tukey's Honest Significant Difference post-hoc test.

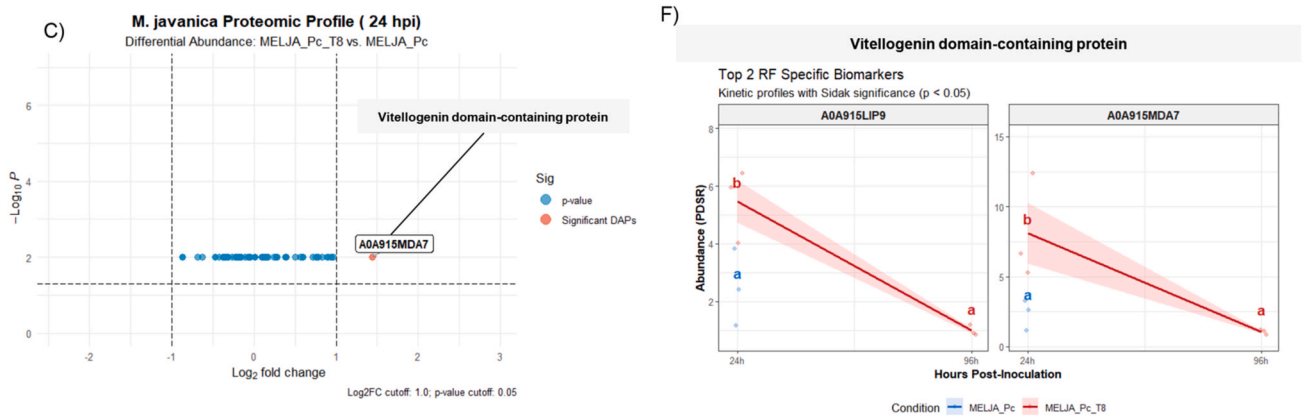


Fig. 15. (*continued*).

- **Surface & Secretion**
- **Energy (Mitochondria)**
- **Structure (Cytoskeleton)**
- **Information (Nucleus/Chromosome)**

This classification enabled a compartment-level interpretation of chitosan's effects.

2.10.6.10. Random forest discrimination within each CC category. RF models were trained for each CC category (see Table 4). Their performance metrics were:

2.10.6.10.1. Interpretation.

- **Energy (Mitochondria)** showed the highest accuracy (50%), indicating strong metabolic disruption.
- **Information (Nucleus/Chromosome)** showed moderate accuracy, suggesting partial effects on nuclear processes.
- **Surface & Secretion** and **Structure** showed lower accuracy but contained several of the **top discriminant proteins**, consistent with chitosan interacting directly with egg envelopes and structural components.

2.10.6.11. Integrated interpretation. Across all analyses—DAPs, GO functional enrichment, PLS-DA, RF, SVM, consensus Venn, GLMM validation, and CC-level RF models—a coherent mechanistic picture emerges:

- Chitosan disrupts **host–parasite interface proteins** (Surface & Secretion).
- It induces **metabolic stress and mitochondrial remodelling** (Energy).
- It affects **structural integrity** (Cytoskeleton).
- Nuclear processes remain comparatively stable.
- A core set of **13 consensus proteins** and **two RF-exclusive drivers** consistently respond to chitosan across all analytical layers.

All machine-learning workflows applied to the *M. javanica* proteome—including RF (executed with fixed seeds for reproducibility), PLS-DA, SVM, consensus modelling, GLMM validation, and Cellular Component functional profiling—were conducted using R v4.4.3 [43].

3. Results

3.1. Early germination and parasitism stages of Pochonia chlamydosporia 123 under chitosan and nematode egg cues

P. chlamydosporia 123 (Pc123) germination at 24 h post-inoculation (hpi) depended strongly on surface hydrophobicity. Conidia germinated more efficiently on hydrophobic polystyrene than on hydrophilic glass, both in sterile distilled water (SDW) and in saline buffer (STC) (Fig. 2A and B). The presence of *Meloidogyne javanica* eggs (RKN100) significantly increased germination on glass, indicating that egg-derived cues can partially compensate for the lack of hydrophobicity. In contrast, the same egg concentration reduced germination on polystyrene (Fig. 2A), suggesting that the effect of eggs on germination is surface-dependent.

Chitosan (T8, 1 mg/mL) significantly reduced Pc123 germination on polystyrene after 24 hpi (2-way ANOVA, $F_{1,36} = 177.7$, $p < 0.001$) (Fig. 2C and D). When Pc123 was incubated with RKN eggs, germination decreased further in the presence of chitosan. However, increasing egg density progressively restored germination levels (Fig. 2C), indicating that egg-derived signals can partially counteract the inhibitory effect of chitosan.

Pc123 conidia suspended in STC buffer successfully approached and adhered to the nematode eggshell surface (Figure S.1A.4). Observations using Pc123 protoplasts indicated that initial host sensing, directional growth, and early adhesion occur even in the absence of the fungal cell wall (FCW). This suggests that plasma membrane components and/or residual extracellular matrix molecules may mediate these primary contact events. Time-course microscopic visualization (Figure S.1A.5) revealed that while protoplasts remained wall-less on the eggshell exterior, internal fungal growth was detectable within the egg as early as 16 hpi. Histochemical staining confirmed that protoplasts adhered to and breached the eggshell, initiating infection prior to FCW regeneration. Following successful penetration, full germination and complete restoration of the FCW were observed within the egg (Fig. 2E).

Although protoplasts are capable of infecting eggs, conidia possessing an intact FCW infected more rapidly. Using the Pc123-GFP strain, fluorescence at 24 hpi localized around the eggshell surface, indicating early adhesion (Fig. 2F). In contrast, eggs infected with normal conidia showed strong internal fluorescence occupying most of the egg volume, demonstrating faster penetration and more extensive internal colonization compared with protoplasts.

3.2. Proteome-wide restructuring and multivariate identification of key drivers in Pc123

The proteome of *P. chlamydosporia* 123 (Pc123) showed extensive restructuring across conditions involving chitosan (T8) and *M. javanica* eggs (RKN). UMAP clustering revealed a clear separation between

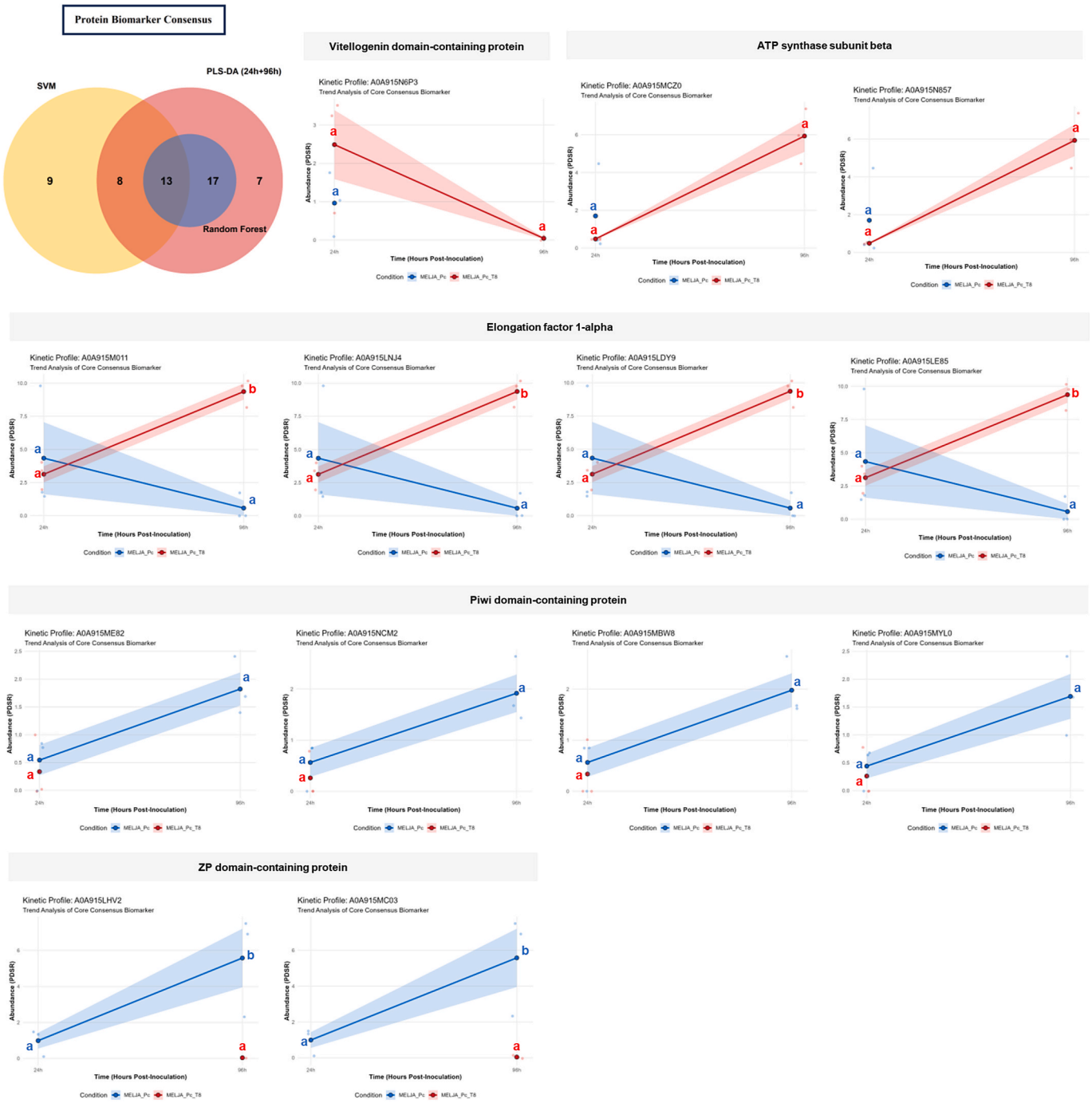


Fig. 16. Consensus biomarker discovery and functional kinetic profiling of the Meloidogyne javanica response. The figure integrates statistical prioritization from three independent machine learning algorithms (SVM, RF, and PLS-DA) to identify and characterize the core proteomic drivers of the nematode response under chitosan-mediated modulation during fungal parasitism. Protein Biomarker Consensus (Top-left): Venn diagram illustrating the overlap between **SVM** (top 30), **RF** (top 30), and **PLS-DA** (top 60; 30 per time point). The intersection identifies 13 core consensus biomarkers, representing the most robust biological signals across all mathematical models. **Kinetic Trend Analysis of Consensus Families:** Evolution of protein abundance (***PDSR***) across experimental conditions: 1) **Vitellogenin domain-containing proteins (Top-Center; A0A915N6P3):** Detected at 24 hpi in both conditions, these proteins persist at 96 hpi only in the **MELJA_Pc_T8** group, albeit with a significant decline.; 2) **ATP synthase subunit beta (Top-right; A0A915MCZ0, A0A915N857):** These bioenergetic markers show a significant abundance increase at 96 hpi exclusively under chitosan treatment, whereas they are undetected in the control (MELJA_Pc); 3) **Elongation factor 1-alpha (Center-top; EF-1α, four isoforms):** Profiles show a sharp increase from 24 to 96 hpi in the **MELJA_Pc_T8** group, contrasting with a decrease in the control, signalling divergent protein synthesis regulation; 4) **Piwi domain-containing proteins (Center-bottom; four isoforms):** These regulators increase at 96 hpi in the control but are suppressed by chitosan, suggesting interference with the nematode's gene-silencing mechanisms; ZP domain-containing proteins (Bottom-left; A0A915LHV2, A0A915MC03): These extracellular matrix proteins exhibit a strong increase at 96 hpi in the control, but remain at low or undetectable levels in the T8 group. **Statistical Validation:** Distinct letters (a, b) in the kinetic plots denote significant differences ($p < 0.05$) between conditions and time points based on **GLMM** followed by **Sidak's post-hoc** tests. Shaded areas represent the 95% confidence intervals for the predicted trends. Abbreviations: GLMM, Generalized Linear Mixed Model; hpi: Hours Post-Inoculation; PLS-DA, Partial Least Squares Discriminant Analysis; RF: Random Forest; Sidak: Sidak's correction for multiple comparisons; SVM: Support Vector Machine; ZP: Zona Pellucida domain.

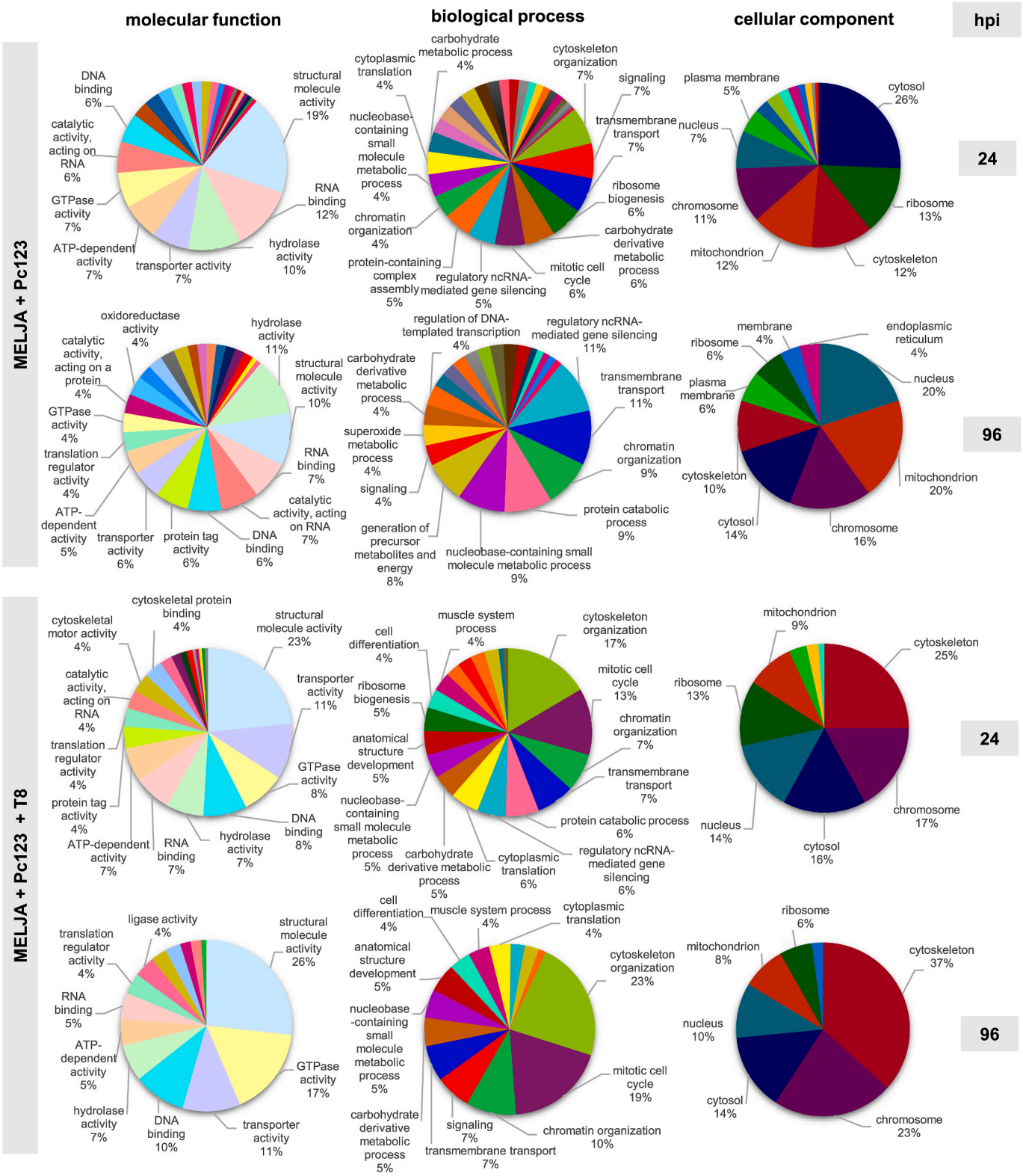


Fig. 17. Gene Ontology (GO) functional distribution of Meloidogyne javanica proteins during interaction with *Pochonia chlamydosporia* and chitosan. Functional annotation of the Meloidogyne javanica (MELJA) egg proteome during interaction with the nematophagous fungus ***P. chlamydosporia*** **(Pc123)** and **Chitosan T8**. The analysis, performed via OmicsBox, highlights the most represented **GO terms** across the three main categories: Biological Process (BP), Molecular Function (MF), and Cellular Component (CC). **Only GO terms accounting for 4% or more of the total annotated proteins are displayed** to identify the primary metabolic and structural shifts induced by the treatments. Abbreviation: hpi, hours post-inoculation.

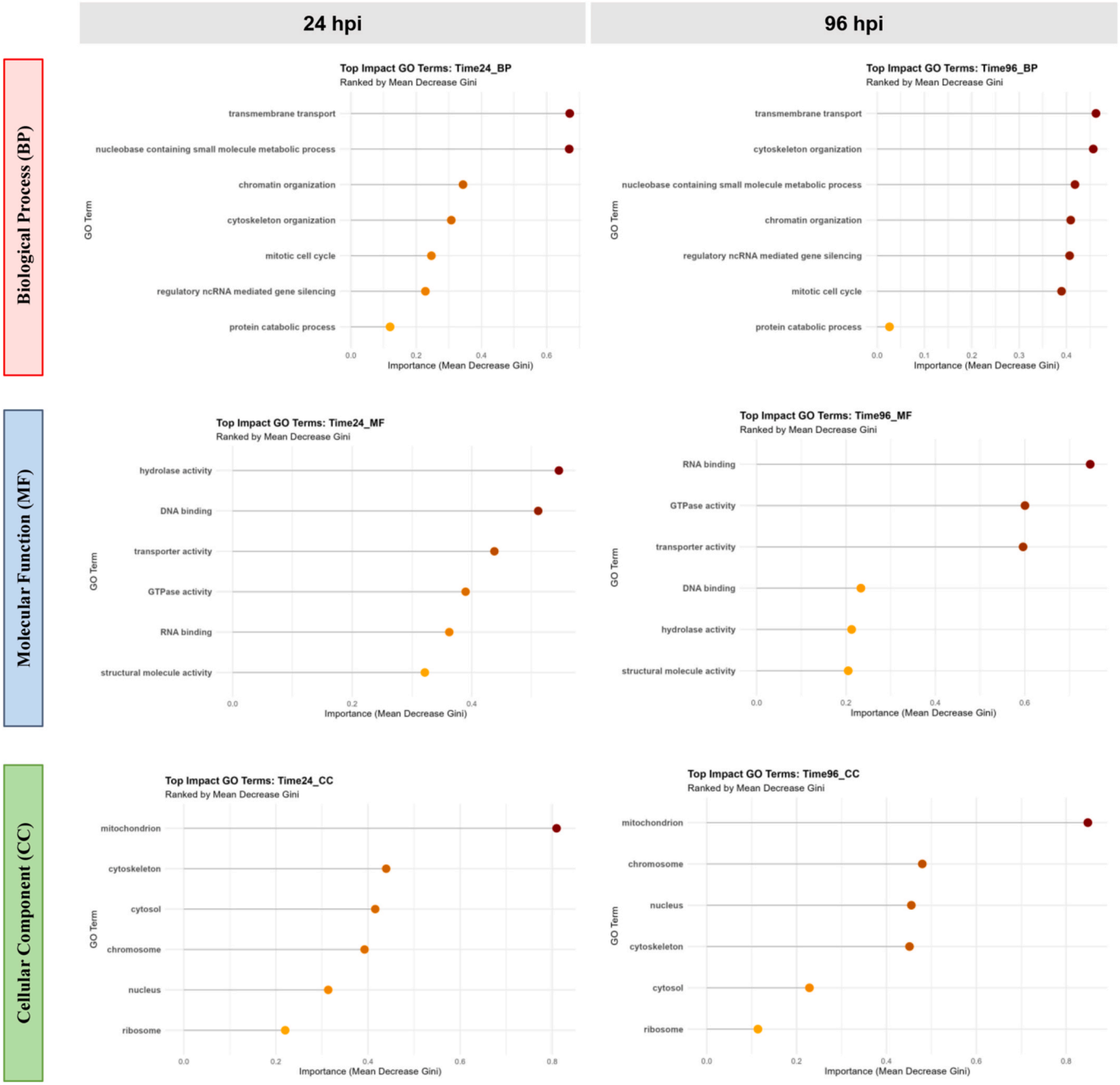


Fig. 18. Random Forest (RF) classification and functional divergence of Meloidogyne javanica GO-term biomarkers. Predictive modelling of functional profiles: RF-based prioritization of **Gene Ontology (GO)** terms from *M. javanica* (**MELJA**) eggs during interaction with ***P. chlamydosporia*** and **chitosan**. Analysis was restricted to **GO terms representing 8% or higher** in at least one condition. Performance metrics (Table 2) indicate a temporal shift from functional overlap at **24 hpi** to strong divergence at **96 hpi**. Abbreviations: hpi, hours post-infection.

scenarios and time points, with chitosan-treated samples showing high similarity at 96 hpi (92.4% between PcT8 and PcRKNT8), indicating a strong convergence of their proteomic profiles (Fig. 3A and B; Table S.11A).

Differentially abundant protein (DAP) analysis showed a temporal expansion of the response (Fig. 3C; Table S.12A). At 24 hpi, all treatments displayed predominantly inductive patterns. By 96 hpi, the regulatory profiles differed: PcRKNT8 retained a large stable core (563 proteins), whereas PcT8 exhibited a higher proportion of repressed proteins, reflecting distinct late-stage proteomic adjustments under prolonged chitosan exposure.

Multivariate modelling supported these observations. A linear SVM classifier (79.2% accuracy; Table S.12B) separated early and late proteomes. PLS-DA indicated that the top 30 VIP proteins at 24 and 96 hpi were non-overlapping: early VIPs (e.g., **ATP synthase subunit alpha**, **mitochondrial porin**) were associated with energy-related categories, while late VIPs (e.g., **1,3-β-glucanosyltransferase**) corresponded to cell-wall-associated terms (Fig. 4; Figure S12C). Random Forest (RF) analysis identified six major discriminant proteins, led by **HSP70–1**, which showed time-dependent variation across treatments (Fig. 5).

Together, these eight consensus biomarkers outline early and late proteomic signatures in Pc123, with **ATP synthase α** and **glycerol kinase** contributing to early **energy-associated profiles**, and **cell-wall-related enzymes** such as β-glucosidase characterizing later stages (Fig. 6).



Fig. 19. Category-specific Random Forest (RF) modelling and expression dynamics of *M. javanica* cellular component biomarkers. Predictive modelling and protein discriminant power: Targeted RF analysis was performed on four major Cellular Component (CC) groups to prioritize the most influential proteins separating the experimental conditions. For each category, the **Mean Decrease Gini (A)** indicates the protein's discriminant importance, while the **bubble plots (B)** illustrate the subcellular expression dynamics across time points (24 and 96 hpi) for the control (MELJA_Pc) and chitosan-treated (MELJA_Pc_T8) eggs. **Energy (Mitochondria):** High-importance predictors include ATP synthase beta isoforms (e.g., A0A915MCZ0, A0A915N857), identifying mitochondrial-associated features as primary sources of variance. **Information (Nucleus/Chromosome):** Seven Global RF consensus proteins (highlighted in blue), including multiple histone variants (e.g., A0A915LJX1, A0A915LIZ7), rank as top discriminant features, reflecting chromatin-level proteomic shifts. **Structure (Cytoskeleton):** This group is dominated

by tubulin α-chains and myosin-tail proteins, consistent with the strong cytoskeletal divergence observed in the global GO profiles. **Surface & Secretion:** The ZP-domain protein (A0A915LHV2) emerged as the top predictor. Proteins highlighted in orange represent specific Surface & Secretion candidates showing treatment-dependent shifts, such as galectins (detected at 24 hpi in control) and VWFA-domain proteins appearing exclusively at 96 hpi in MELJA_Pc. **Legend and Comparative Metrics:** Blue highlights denote proteins belonging to the **MELJA Global RF Top 30** discriminant features. Orange highlights represent **Surface & Secretion** proteins exhibiting significant treatment-specific abundance shifts. Directional trend indicators (arrows/cartoons) represent abundance shifts relative to the parasitism control (**MELJA_Pc**, pink) and temporal shifts compared to the 24h baseline within the same condition (**gold**). Schematic illustrations were created using BioRender.com. The chemical structure of chitosan was modelled based on Chitosan from shrimp shells (PubChem CID 71853). Abbreviations: ***PDSR***, Protein Detection Success Rate; **ZP**, Zona Pellucida; **VWFA**, Von Willebrand Factor type A. (For interpretation of the references to colour in this figure legend, the reader is referred to the Web version of this article.)

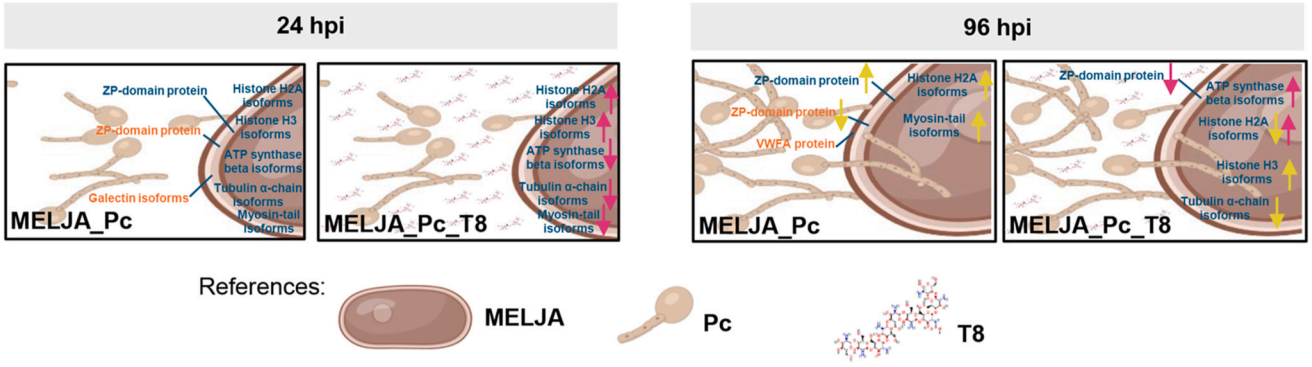


Fig. 19. (*continued*).

3.3. Functional proteome plasticity of Pochonia chlamydosporia under stress

Functional annotation (Figs. 7 and 8) showed stimulus-dependent differences in Pc123 proteomic profiles. At **24 hpi**, the response was dominated by categories associated with **translational processes**. Molecular Function terms were enriched in structural molecule activity (21–27%) and RNA binding (14–19%), while Cellular Component (CC) annotation indicated that ribosomal and cytosolic proteins accounted for up to 66% of the proteome, a higher proportion than in the control.

By **96 hpi**, the functional distribution shifted toward categories linked to **catabolic and metabolic processes**. Hydrolase activity (14–17%) and amino-acid-related terms increased, particularly in the **PcRKNT8** treatment. This shift coincided with a rise in mitochondrial-associated proteins, which reached 19% of the annotated CC terms.

Statistical validation and RF classification (accuracy >66%) supported these temporal differences (Fig. 9). At 24 hpi, **lipid metabolic processes** and **transmembrane transport** were the most discriminant BP terms, whereas at 96 hpi, **hydrolase activity** (MF) and **extracellular region** and **mitochondrion** (CC) emerged as the top discriminants. These functional signatures outline distinct early and late proteomic profiles in Pc123 under the different treatments, without implying functional outcomes beyond the observed *in vitro* protein distributions.

3.4. Structural and functional reconfiguration of the Pc123 secretory proteome

The analysis of Pc123 **proteins containing non-cytoplasmic domains** revealed stimulus-dependent differences under chitosan (T8) and *M. javanica* eggs (RKN). At **24 hpi**, proteins containing signal peptides (SP) and transmembrane helices (TM) were more frequently detected in PcRKN and PcT8 compared with the control, indicating early activation of secretion-associated and membrane-related categories. By **96 hpi**, **PcRKNT8** showed the highest cumulative detection of proteins annotated with secretory features, reflecting a marked expansion of the secretory repertoire in the combined treatment (Fig. 10).

3.4.1. Sequence–feature space and phylogenetic convergence

To evaluate the origin of structural variation in non-cytoplasmic proteins, we compared three independent biological signals: localization-driven distances derived from the Non-Cyt domain, global evolutionary divergence from the full peptide sequence, and vector-based structural distances obtained from sequence-feature composition. This comparison allowed us to determine which signal best explained the organization of the Pc123 secretome across treatments and time points.

Sequence–feature clustering (Fig. 11; Supplementary S.14) showed that early responses (24 hpi) in Pc and PcT8 were enriched in SP-rich proteins associated with cell-wall remodelling and carbohydrate metabolism, whereas PcRKN displayed a predominance of TM-associated proteins. These patterns were consistent with the structural variation captured by the sequence-feature vectors, indicating that the Non-Cyt domain encodes biologically meaningful localization-driven information.

Mantel and cophenetic correlations between structural-feature distances and phylogenetic distances derived from both Non-Cyt and full-sequence trees (Table 3; phylogenetic trees in Supplementary S.14) revealed a consistent pattern across scenarios: **localization-driven Non-Cyt distances and vector-based structural distances aligned more strongly with each other than with evolutionary distances**, indicating that **structural organization in the Pc123 secretome is primarily driven by localization-encoded and sequence-feature signals rather than by evolutionary proximity**. Both Non-Cyt and full-sequence evolutionary distances showed low and non-significant correlations with structural-feature space in most treatments.

The only exception was **PcRKNT8 at 96 hpi**, where full-sequence evolutionary distances showed a **significant correlation** with structural-feature variation. This indicates that under combined RKN + chitosan stress, **a conserved, evolutionarily coherent subset of secretory proteins is mobilized**, partially overriding the otherwise dominant localization-driven organization.

3.4.2. Machine-learning prediction of cellular localization

The RF Global model trained on GO.db CC annotations (*OBB* 50%; 2000 trees; Fig. 12) identified the **Top 20 most discriminant Non-Cyt proteins** across all treatments and time points. These included extracellular hydrolases (e.g., glucanases, GH18 chitinases), cell-wall-associated proteins (CWP1–3), and stress-related enzymes such as catalase and oxalate decarboxylase. All RF-derived candidates were statistically validated using Gamma GLMMs with Tukey-adjusted contrasts.

To resolve spatial organization, four additional RF models were trained independently for each major Cellular Component (CC) category—Extracellular, Membrane, Cytoplasmic, and Intracellular/Organelle—using OmicsBox annotations (Figs. 13 and 14). Each model produced **Top 10 discriminant proteins** and revealed strong temporal differentiation (24 vs. 96 hpi) in extracellular and membrane compartments.

A **consensus analysis** between the RF Global model and the CC-specific RFs identified a **stable core of six extracellular drivers**, all of which appear in both the global Top 20 and the Extracellular Top 10 (Fig. 13). These include:

- A0A4Q7JLT6 (**Glucan 1,3-β-glucosidase**)
- A0A4V2EPG1 (**CFEM domain-containing protein 1**)
- A0A4Q7JQ33 (**Heterokaryon incompatibility protein**)
- A0A4Q7JT25 (**GH18 chitinase**)
- A0A4Q7JXI7 (**Glycosidase 1**)
- A0A4Q7JPW1 (**Cell wall protein 3**)

Within this consensus set, **A0A4Q7JLT6** was the **top-ranked driver**, as it was simultaneously the highest-importance feature in the **RF-Extracellular model** and one of the strongest predictors in the **RF Global model**.

In contrast, no consensus proteins were detected for the **Membrane** group, indicating that membrane-associated signals arise from a distinct and more heterogeneous subset. The membrane RF highlighted proteins such as A0A4Q7K1K2 (**Cupin-type protein**), A0A4Q7K4R2 (**Putative adhesin**), and A0A4Q7KA57 (**Copper acquisition factor BIM1-like**), which were abundant but did not overlap with the global RF drivers (Fig. 13).

Intracellular and Cytoplasmic compartments showed more stable internal profiles (Fig. 14). The **Intracellular/Organelle** RF was led by A0A4Q7JUA9 (**Methylmalonate-semialdehyde dehydrogenase**), while the Cytoplasmic RF was dominated by A0A4Q7JTB1 (**Formate dehydrogenase**). Only a small subset of these proteins overlapped with the global Top 20, reflecting compartment-specific functional specialization.

Together, these analyses demonstrate that **the Pc123 secretome contains a robust, cross-validated core of extracellular drivers**, with A0A4Q7JLT6 acting as the leading contributor, while membrane-associated proteins follow a separate, non-overlapping trajectory.

3.5. Chitosan-induced restructuring of the Meloidogyne javanica proteome

To compare the proteomic profiles of *M. javanica* during *P. chlamydosporia* parasitism, we analysed samples obtained in the absence (MELJA_Pc) and presence of chitosan (MELJA_Pc_T8). UMAP and shared-protein analyses showed that the proteomes were 56.6% similar at 24 hpi but decreased to 19.3% similarity by 96 hpi, reflecting a marked time-dependent divergence between the two conditions (Fig. 15A and B).

3.5.1. Differential abundance and consensus biomarkers

At **24 hpi**, the nematode proteome showed high stability, with only one protein, **A0A915MDA7 (Vitellogenin)**, significantly up-regulated under chitosan exposure (Fig. 15C). By **96 hpi**, six differentially abundant proteins were detected. Four **Elongation factor 1-alpha** isoforms (EF-1α; A0A915LDY9, A0A915LNJ4, A0A915LE85, A0A915M011) displayed >6-fold increases, whereas two **ZP-domain proteins** (A0A915LHV2, A0A915MC03) were reduced in abundance in the chitosan treatment (Fig. 15D).

A **Global RF model** independently identified two vitellogenins as the most discriminant features separating the two conditions (Fig. 15E and F). Integration of the top-ranked proteins from **RF, SVM, and PLS-DA** yielded a set of **13 consensus biomarkers** that characterize the proteomic differences observed between treatments (Fig. 16). These biomarkers—including **ATP synthase subunit beta, EF1-α, Piwi, and ZP-domain proteins**—reflect coordinated changes in reproductive, energetic, and structural pathways, outlining a molecular signature associated with the chitosan-modulated interaction between *Pc123* and *M. javanica*.

3.5.2. Functional reprogramming and GO-term modelling

Functional enrichment analysis (Fig. 17) revealed marked, condition-dependent shifts in Molecular Function (MF), Biological Process (BP), and Cellular Component (CC). **RF GO-term modelling** (Fig. 18) identified that at 24 hpi, both proteomes were dominated by structural molecule activity (19% in MELJA_Pc; 23% in MELJA_Pc_T8). However, while the control (MELJA_Pc) showed enrichment in transmembrane signalling, the chitosan-treated eggs (MELJA_Pc_T8) displayed higher representation of **cytokinesis (17%) and mitotic cell cycle (13%)** categories, indicating an early divergence in the functional profile associated with cell-division-related processes.

By 96 hpi, a clear divergence in GO-term representation was observed. The control proteome showed increased abundance of categories related to **ncRNA-mediated gene silencing (11%)** and proteins with nuclear or mitochondrial localization, whereas MELJA_Pc_T8 displayed higher representation of **cytoskeletal components (17%)** and **chromosomal-associated terms (23%)**. RF analysis of CC categories identified **mitochondrial-associated** features as the most discriminant variables separating the two conditions.

3.5.3. Targeted RF analysis of cellular component drivers

To further characterize the proteomic differences between conditions, we performed **category-specific RF modelling** (Fig. 19) on four CC-related protein groups. This analysis placed the **Global RF consensus** proteins within their corresponding functional categories.

- ***Energy (Mitochondria):*** ATP synthase beta isoforms (**A0A915MCZ0**, **A0A915N857**) were the top predictors, indicating that mitochondrial-associated proteins contributed strongly to separating the two conditions.
- ***Information (Nucleus/Chromosome):*** Seven Global RF proteins, including several **histone variants** (e.g., **A0A915LJX1**, **A0A915LIZ7**), ranked among the most discriminant features, reflecting differences in chromatin-associated categories.
- ***Structure (Cytoskeleton):*** **Tubulin α-chains** (A0A915M7V8, A0A915LSW8) and **myosin-tail** proteins (A0A915LEA2, A0A915LGR0) dominated this group, consistent with the cytoskeleton-related terms identified in the GO profiles.
- ***Surface & Secretion:*** The **ZP-domain protein A0A915LHV2** was the top predictor in this category. Additional condition-specific patterns were observed, such as **galectins** (A0A915N872, A0A915LXQ3) detected only in MELJA_Pc at 24 hpi, and **VWFA-domain proteins** appearing exclusively at 96 hpi in the absence of chitosan.

Together, these RF-derived patterns outline distinct proteomic signatures between treatments, particularly in mitochondrial, chromosomal, cytoskeletal, and surface-associated categories, without implying functional outcomes beyond the observed *in vitro* protein distributions.

4. Discussion

Recent studies highlight the urgent need for sustainable nematode management strategies, including nanomaterials [10], botanical extracts [8], and integrated biocontrol approaches [9]. Within this context, *P. chlamydosporia* has emerged as a promising biological control agent [18,44], yet the molecular mechanisms underlying its parasitism and its interaction with elicitors such as chitosan remain poorly understood. Our integrative proteomic, microscopic, and machine-learning analyses

provide new insights into this tripartite system.

4.1. Integration of surface and host signals during early colonization

Our findings underscore the remarkable phenotypic plasticity of *P. chlamydosporia* during its transition from a saprotrophic to a parasitic state. The fungus does not merely react to surface hydrophobicity [16,35], but executes a "host-sensing" program. The ability of *M. javanica* eggs to trigger germination on hydrophilic substrates suggests that host-derived chemical cues may modulate or partially override physical constraints. Furthermore, the accelerated infection kinetics in saline suspension—compared to previous agar-based reports [17] (Supplementary Data S.1A.5)—highlights that liquid microenvironments may optimize the diffusion of fungal effectors and the subsequent enzymatic softening of the eggshell.

4.2. Temporal proteomic architecture: from priming to parasitism

The proteomic landscape of Pc123 is defined by a highly resolved temporal hierarchy. The initial response (24 hpi) represents a **translational priming phase**, characterized by an up-regulation of the protein synthesis machinery and early virulence-associated factors [45,46]. As the interaction progresses to 96 hpi, the fungus displays a shift toward a more **catabolic and degradative proteomic profile**. Our multivariate models (PLS-DA and Random Forest) **identified HSP70** [47], **ATP synthase** [15], **and secreted proteases** [12,14] as key contributors to this transition. This temporal reconfiguration is consistent with the metabolic demands **expected during sustained growth and nutrient acquisition** in fungal–nematode interactions [48].

4.3. Chitosan as a metabolic elicitor of fungal virulence

A central finding of this study is the dual role of chitosan as both a stressor and an elicitor. Chitosan imposes a physiological constraint that leads Pc123 to restructure its membrane-associated and secretory processes [25,28]. Rather than inhibiting the fungus, chitosan is associated with a proteomic profile indicative of enhanced "parasitic readiness," including the increased representation of **carbohydrate-active enzymes** (CAZymes) and **extracellular hydrolases**. The emergence of **extracellular glucanases** and **CFEM-domain proteins** as top predictors in our machine-learning models suggests that chitosan modulates the secretory repertoire of Pc123 in ways that may influence, or at least coincide with, its interaction with the multilayered structure of the nematode eggshell [13,19,49–51].

4.4. Destabilization of nematode resilience pathways

The tripartite interaction (MELJA_Pc_T8) reveals (Figs. 15–19; S16) that chitosan is associated with proteomic changes in the nematode that involve pathways linked to structural and defensive integrity. Our proteomic analysis of MELJA suggests a three-pronged impact:

1. **Reproductive Provisioning:** The early perturbation of **vitellogenins** indicates alterations in proteins involved in embryonic provisioning [52].
2. **Structural Components:** The significant suppression of **ZP-domain proteins**—essential components of the eggshell extracellular matrix [53,54]—suggests changes that may influence the structural environment of the egg during fungal interaction.
3. **Metabolic Stress:** At 96 hpi, the shift toward **oxidative stress markers** and **ATP synthase beta-subunits** reflects a proteomic signature consistent with increased metabolic demand, particularly under chitosan exposure [55–57].

While Pc123 alone induces a standard stress-related proteomic response in the host, the addition of chitosan coincides with a broader reconfiguration of nematode pathways associated with reproduction, structure, and metabolism, which may influence the physiological context in which parasitism occurs.

4.5. Concluding remarks: A molecular framework for synergistic biocontrol

In conclusion, the synergy between *P. chlamydosporia* and chitosan can be interpreted as a coordinated "push–pull" interaction: chitosan "pushes" the fungus toward a secretory and metabolic program consistent with parasitism, while simultaneously coinciding with proteomic changes in *M. javanica* that affect structural and reproductive pathways. This integrative perspective, combining high-resolution proteomics with machine-learning validation, provides a molecular framework that may inform the development of next-generation bionematicides within the paradigm of sustainable plant pathology [2].

5. Conclusion

This study establishes that chitosan acts as a powerful orchestrator of the tripartite interaction between *Pochonia chlamydosporia* 123 and *Meloidogyne javanica*. We demonstrate that while fungal germination and initial infection are governed by host-derived and physical cues, chitosan progressively shifts the fungal proteome toward a high-energy parasitic program characterized by mitochondrial activation and an expanded secretory repertoire. Simultaneously, chitosan coincides with proteomic alterations in the nematode that affect reproductive and structural pathways, changes that may influence the eggshell environment during parasitism.

Notably, the integration of machine-learning architectures (Random Forest, SVM, and PLS-DA) proved indispensable for identifying robust biomarkers and functional signatures that remain obscured under conventional statistical frameworks. These computational approaches provide a predictive molecular map of enhanced parasitism, offering a scalable framework for optimizing the efficacy of chitosan-based bionematicides in sustainable agriculture.

Fundings

This research was funded by PID2020–119734RB-I00 Project from the Spanish Ministry of Science and Cropsafe Project 101209410 from the EU CBE JU.

CRediT authorship contribution statement

C.M. Berosich: Conceptualization, Data curation, Formal analysis, Investigation, Methodology, Resources, Software, Validation, Visualization, Writing – original draft, Writing – review & editing. **M. Valverde-Urrea:** Formal analysis. **J.J. Zubcoff:** Methodology, Software, Supervision, Validation, Writing – review & editing. **L.V. Lopez-Llorca:** Conceptualization, Funding acquisition, Methodology, Project administration, Resources, Writing – review & editing. **F. Lopez-Moya:** Conceptualization, Funding acquisition, Methodology, Project administration, Resources, Supervision, Writing – review & editing.

Declaration of competing interest

The authors declare that they have no known competing financial interests or personal relationships that could have appeared to influence the work reported in this paper. All authors have approved the final version and agree to its submission. We have no conflicts of interest to disclose.

Acknowledges

We would like to thank Dr. Susana Sellés Marchart and Mari Merce

Cascant Vilaplana from the Genomics and Proteomics Unit of the Common Research Facilities (SSTTi) of the University of Alicante for their collaboration in the isolation and detection of proteins.

Appendix A. Supplementary data

Supplementary data to this article can be found online at https://doi.org/10.1016/j.pmpp.2026.103287.

Data availability

Data will be made available on request.

References

[1] J.T. Jones, A. Haegeman, E.G.J. Danchin, H.S. Gaur, J. Helder, M.G.K. Jones, T. Kikuchi, R. Manzanilla-López, J.E. Palomares-Rius, W.M.L. Wesemael, R. N. Perry, Top 10 plant-parasitic nematodes in molecular plant pathology, Mol. Plant Pathol. 14 (2013) 946–961, https://doi.org/10.1111/mpp.12057.

[2] A. Afzal, T. Mukhtar, Revolutionizing nematode management to achieve global food security goals—An overview, Heliyon 10 (2024) e25325, https://doi.org/10.1016/j.heliyon.2024.e25325.

[3] C. Kantor, J.D. Eisenback, M. Kantor, Biosecurity risks to human food supply associated with plant-parasitic nematodes, Front. Plant Sci. 15 (2024) 1404335, https://doi.org/10.3389/fpls.2024.1404335.

[4] L.M. Parrado, M. Quintanilla, Plant-parasitic nematode disease complexes as overlooked challenges to crop production, Front. Plant Sci. 15 (2024) 1439951, https://doi.org/10.3389/fpls.2024.1439951.

[5] R.Y. Ghareeb, E.E. Hafez, D.S. Ibrahim, Current management strategies for phytoparasitic nematodes, in: R. Ansari, R. Rizvi, I. Mahmood (Eds.), Management of Phytonematodes: Recent Advances and Future Challenges, Springer, Singapore, 2020, pp. 339–352, https://doi.org/10.1007/978-981-15-4087-5_15.

[6] M. Tariq-Khan, T.U. Rehman, T. Mukhtar, M. Mahmood, A.U. Rahman, R. Ahmed, Population dynamics and virulence patterns of root-knot nematodes (*Meloidogyne* spp.) on tomato in Poonch Highlands, Azad Jammu and Kashmir, Pakistan, J. Phytopathol. 173 (2025) e70060, https://doi.org/10.1111/jph.70060.

[7] I. Yaseen, T. Mukhtar, Impact of sequential and concurrent inoculations of *Meloidogyne incognita* and *Fusarium oxysporum* f. sp. *vasinfectum* on the growth performance of diverse okra cultivars, Plant Prot. 8 (2024) 303–313, https://doi.org/10.33804/pp.008.02.5186.

[8] W. Azeem, T. Mukhtar, M.I. Haq, M.A. Khan, M.S. Ibrahim, A. Hassan, H. Regmi, L. W. Duncan, The nematicidal potential of *Moringa oleifera* extracts and rhizobacteria against *Meloidogyne incognita* in tomato, Front. Plant Sci. 16 (2025) 1562074, https://doi.org/10.3389/fpls.2025.1562074.

[9] M. Saeed, T. Mukhtar, R. Ahmed, U. Mehmood, M.A. Iqbal, Synergistic efficacy of *Azadirachta indica* and biocontrol agents in mitigating *Meloidogyne javanica* infection in peach, Australas. Plant Pathol. 55 (2026) 14, https://doi.org/10.1007/s13313-026-01104-2.

[10] A. Mehak, A. Akram, A. Ali, N.I. Raja, T. Mukhtar, J.S.S. Seelan, M. Shahbaz, Nano-TiO_2 as a sustainable strategy to control root-knot nematodes (RKNs) in tomato (*Solanum lycopersicum* L.), Physiol. Mol. Plant Pathol. (2026) 103122, https://doi.org/10.1016/j.pmpp.2026.103122, 103122.

[11] L.V. Lopez-Llorca, G.H. Duncan, A study of fungal endoparasitism of the cereal cyst nematode (*Heterodera avenae*) by scanning electron microscopy, Can. J. Microbiol. 34 (1988) 613–619, https://doi.org/10.1139/m88-101.

[12] R. Segers, T.M. Butt, B.R. Kerry, A. Beckett, J.F. Peberdy, The role of the proteinase VCP1 produced by the nematophagous *Verticillium chlamydosporium* in the infection process of nematode eggs, Mycol. Res. 100 (1996) 421–428, https://doi.org/10.1016/S0953-7562(96)80138-9.

[13] V.E. Tikhonov, L.V. Lopez-Llorca, J. Salinas, H.-B. Jansson, Purification and characterization of chitinases from the nematophagous fungi *Verticillium chlamydosporium* and *V. suchlasporium*, Fungal Genet. Biol. 35 (2002) 67–78, https://doi.org/10.1006/fgbi.2001.1312.

[14] L.V. Lopez-Llorca, S. Gómez-Vidal, E. Monfort, E. Larriba, J. Casado-Vela, F. Elortza, H.-B. Jansson, J. Salinas, J. Martín-Nieto, Expression of serine proteases in egg-parasitic nematophagous fungi during barley root colonization, Fungal Genet. Biol. 47 (2010) 342–351, https://doi.org/10.1016/j.fgb.2010.01.004.

[15] L.C. Rosso, M.M. Finetti-Sialer, P.R. Hirsch, A. Ciancio, B.R. Kerry, I.M. Clark, Transcriptome analysis shows differential gene expression in the saprotrophic to parasitic transition of *Pochonia chlamydosporia*, Appl. Microbiol. Biotechnol. 90 (2011) 1981–1994, https://doi.org/10.1007/s00253-011-3282-7.

[16] N. Escudero, S.R. Ferreira, F. Lopez-Moya, M.A. Naranjo-Ortiz, A.I. Marin-Ortiz, C. R. Thornton, L.V. Lopez-Llorca, Chitosan enhances parasitism of *Meloidogyne javanica* eggs by the nematophagous fungus *Pochonia chlamydosporia*, Fungal Biol. 120 (2016) 572–585, https://doi.org/10.1016/j.funbio.2015.12.005.

[17] N. Escudero, L.V. Lopez-Llorca, Effects on plant growth and root-knot nematode infection of an endophytic GFP transformant of the nematophagous fungus *Pochonia chlamydosporia*, Symbiosis 57 (2012) 33–42, https://doi.org/10.1007/s13199-012-0173-3.

[18] T. Mukhtar, M.A. Hussain, M.Z. Kayani, Biocontrol potential of *Pasteuria penetrans, Pochonia chlamydosporia, Paecilomyces lilacinus* and *Trichoderma harzianum* against *Meloidogyne incognita* in okra, Phytopathol. Mediterr. 52 (2013) 66–76. http://www.jstor.org/stable/42685384.

[19] A. Aranda-Martinez, N. Lenfant, N. Escudero, E.A. Zavala-Gonzalez, B. Henrissat, L. V. Lopez-Llorca, CAZyme content of *Pochonia chlamydosporia* reflects that chitin and chitosan modification are involved in nematode parasitism, Environ. Microbiol. 18 (2016) 4200–4215, https://doi.org/10.1111/1462-2920.13544.

[20] F. Lopez-Moya, M. Suarez-Fernandez, L.V. Lopez-Llorca, Molecular mechanisms of chitosan interactions with fungi and plants, Int. J. Mol. Sci. 20 (2019) 332, https://doi.org/10.3390/ijms20020332.

[21] J. Liu, S. Tian, X. Meng, Y. Xu, Effects of chitosan on control of postharvest diseases and physiological responses of tomato fruit, Postharvest Biol. Technol. 44 (2007) 300–306, https://doi.org/10.1016/j.postharvbio.2006.12.019.

[22] J. Palma-Guerrero, H.-B. Jansson, J. Salinas, L.V. Lopez-Llorca, Effect of chitosan on hyphal growth and spore germination of plant pathogenic and biocontrol fungi, J. Appl. Microbiol. 104 (2008) 541–553, https://doi.org/10.1111/j.1365-2672.2007.03567.x.

[23] F. Lopez-Moya, D. Kowbel, M.J. Nueda, J. Palma-Guerrero, N.L. Glass, L.V. Lopez-Llorca, *Neurospora crassa* transcriptomics reveals oxidative stress and plasma membrane homeostasis biology genes as key targets in response to chitosan, Mol. Biosyst. 12 (2016) 391–403, https://doi.org/10.1039/C5MB00649J.

[24] D. Meng, G. Betchem, Y. Ren, M. Yao, X. Xia, M. Li, Y. Wang, Antifungal activity of chitosan against *Aspergillus ochraceus* and its possible mechanisms of action, Int. J. Biol. Macromol. 158 (2020) 1063–1070, https://doi.org/10.1016/j.ijbiomac.2020.04.213.

[25] J. Palma-Guerrero, J.A. Lopez-Jimenez, A.J. Pérez-Berná, I.-C. Huang, H.-B. Jansson, J. Salinas, L.V. Lopez-Llorca, Membrane fluidity determines sensitivity of filamentous fungi to chitosan, Mol. Microbiol. 75 (2010) 1021–1032, https://doi.org/10.1111/j.1365-2958.2009.07039.x.

[26] A. Aranda-Martinez, M.Á. Naranjo-Ortiz, I.S. Abihssira García, E.A. Zavala-Gonzalez, L.V. Lopez-Llorca, Ethanol production from chitosan by the nematophagous fungus *Pochonia chlamydosporia* and the entomopathogenic fungi *Metarhizium anisopliae* and *Beauveria bassiana*, Microbiol. Res. 204 (2017) 30–39, https://doi.org/10.1016/j.micres.2017.07.009.

[27] N. Escudero, F. Lopez-Moya, Z. Ghahremani, E.A. Zavala-Gonzalez, A. Alaguero-Cordovilla, C. Ros-Ibañez, A. Lacasa, F.J. Sorribas, L.V. Lopez-Llorca, Chitosan increases tomato root colonization by *Pochonia chlamydosporia* and their combination reduces root-knot nematode damage, Front. Plant Sci. 8 (2017) 1415, https://doi.org/10.3389/fpls.2017.01415.

[28] M. Suarez-Fernandez, C. Sambles, F. Lopez-Moya, M.J. Nueda, D.J. Studholme, L. V. Lopez-Llorca, Chitosan modulates *Pochonia chlamydosporia* gene expression during nematode egg parasitism, Environ. Microbiol. 23 (2021) 4980–4997, https://doi.org/10.1111/1462-2920.15408.

[29] E. Luna, V. Pastor, J. Robert, V. Flors, B. Mauch-Mani, J. Ton, Callose deposition: a multifaceted plant defense response, Mol. Plant Microbe Interact. 24 (2011) 183–193, https://doi.org/10.1094/MPMI-07-10-0149.

[30] L.A. Hadwiger, Multiple effects of chitosan on plant systems: solid science or hype, Plant Sci. 208 (2013) 42–49, https://doi.org/10.1016/j.plantsci.2013.03.007.

[31] R.S. Riseh, M. Hassanisaadi, M. Vatankhah, S.A. Babaki, E. Ait Barka, Chitosan as a potential natural compound to manage plant diseases, Int. J. Biol. Macromol. 220 (2022) 998–1009, https://doi.org/10.1016/j.ijbiomac.2022.08.109.

[32] C.M. Olivares-Bernabeu, L.V. Lopez-Llorca, Fungal egg-parasites of plant-parasitic nematodes from Spanish soils, Rev. Iberoam. Micol. 19 (2002) 104–110.

[33] J.G. Maciá-Vicente, H.-B. Jansson, N.J. Talbot, L.V. Lopez-Llorca, Real-time PCR quantification and live-cell imaging of endophytic colonization of barley (*Hordeum vulgare*) roots by *Fusarium equiseti* and *Pochonia chlamydosporia*, New Phytol. 182 (2009) 213–228, https://doi.org/10.1111/j.1469-8137.2008.02743.x.

[34] M. Plascencia-Jatomea, G. Viniegra, R. Olayo, M.M. Castillo-Ortega, K. Shirai, Effect of chitosan and temperature on spore germination of *Aspergillus niger*, Macromol. Biosci. 3 (2003) 582–586, https://doi.org/10.1002/mabi.200350024.

[35] L.V. Lopez-Llorca, C. Olivares-Bernabeu, J. Salinas, H.-B. Jansson, P. E. Kolattukudy, Pre-penetration events in fungal parasitism of nematode eggs, Mycol. Res. 106 (2002) 499–506, https://doi.org/10.1017/S0953756202005798.

[36] L.V. Lopez-Llorca, J.G. Maciá-Vicente, H.-B. Jansson, Nematophagous fungi: mode of action and interactions, CAB Rev. 43 (2007) 59.

[37] S.H. Doerr, R.A. Shakesby, R. Walsh, Soil water repellency: its causes, characteristics and hydro-geomorphological significance, Earth Sci. Rev. 51 (2000) 33–65, https://doi.org/10.1016/S0012-8252(00)00011-8.

[38] C.N. Lowe, K.R. Butt, Culture techniques for soil dwelling earthworms: a review, Pedobiologia 49 (2005) 401–413, https://doi.org/10.1016/j.pedobi.2005.04.005.

[39] A. Bensadoun, D. Weinstein, Assay of proteins in the presence of interfering materials, Anal. Biochem. 70 (1976) 241–250, https://doi.org/10.1016/S0003-2697(76)80064-4.

[40] R Core Team, R: a Language and Environment for Statistical Computing, R Foundation for Statistical Computing, Vienna, Austria, 2024. http://www.R-project.org/.

[41] L. Breiman, Random forests, Mach. Learn. 45 (2001) 5–32, https://doi.org/10.1023/A:1010933404324.

[42] A. Liaw, M. Wiener, Classification and regression by randomForest, R. News 2 (2002) 18–22.

[43] R Core Team, R: a Language and Environment for Statistical Computing, R Foundation for Statistical Computing, Vienna, Austria, 2025. https://www.r-project.org/.

[44] C.M. Berosich, F. Lopez-Moya, L.V. Lopez-Llorca, Modulation of the host defence system by nematophagous fungi and chitosan, Encyclopedia 4 (2024) 379–394, https://doi.org/10.3390/encyclopedia4010026.

[45] E. Larriba, M.D. Jaime, J. Carbonell-Caballero, A. Conesa, J. Dopazo, C. Nislow, J. Martín-Nieto, L.V. Lopez-Llorca, Sequencing and functional analysis of the genome of a nematode egg-parasitic fungus, *Pochonia chlamydosporia*, Fungal Genet. Biol. 65 (2014) 69–80, https://doi.org/10.1016/j.fgb.2014.02.002.

[46] R. Lin, F. Qin, B. Shen, Q. Shi, C. Liu, X. Zhang, Y. Jiao, J. Lu, Y. Gao, M. Suarez-Fernandez, F. Lopez-Moya, L.V. Lopez-Llorca, G. Wang, Z. Mao, J. Ling, Y. Yang, X. Cheng, B. Xie, Genome and secretome analysis of *Pochonia chlamydosporia* provide new insight into egg-parasitic mechanisms, Sci. Rep. 8 (2018) 1123, https://doi.org/10.1038/s41598-018-19169-5.

[47] A. De Maio, Extracellular Hsp70: export and function, Curr. Protein Pept. Sci. 15 (2014) 225–231, https://doi.org/10.2174/1389203715666140331113057.

[48] L. Hao, F. Zhao, H. Liu, C. Ma, X. Jia, L. Jiang, Z. Fan, R. Wang, Dynamic proteomic changes and ultrastructural insights into *Pochonia chlamydosporia*'s parasitism of *Parascaris equorum* eggs, Front. Cell. Infect. Microbiol. 15 (2025) 1600620, https://doi.org/10.3389/fcimb.2025.1600620.

[49] I.V. Ene, L.A. Walker, M. Schiavone, K.K. Lee, H. Martin-Yken, E. Dague, N.A. R. Gow, C.A. Munro, A.J.P. Brown, Cell wall remodeling enzymes modulate fungal cell wall elasticity and osmotic stress resistance, mBio 6 (2015), https://doi.org/10.1128/mBio.00986-15 e00986–15.

[50] N.A. Gow, J.P. Latgé, C.A. Munro, The fungal cell wall: structure, biosynthesis, and function, Microbiol. Spectr. 5 (2017), https://doi.org/10.1128/microbiolspec.funk-0035-2016. FUNK-0035-2016.

[51] N.A. Gow, M.D. Lenardon, Architecture of the dynamic fungal cell wall, Nat. Rev. Microbiol. 21 (2023) 248–259, https://doi.org/10.1038/s41579-022-00796-9.

[52] H. Li, S. Zhang, Functions of vitellogenin in eggs, in: M. Kloc (Ed.), Oocytes. Results and Problems in Cell Differentiation, 63, Springer, Cham, 2017, pp. 1–20, https://doi.org/10.1007/978-3-319-60855-6_17.

[53] A.F. Bird, M.A. McClure, The tylenchid (Nematoda) egg shell: structure, composition and permeability, Parasitology 72 (1976) 19–28, https://doi.org/10.1017/S0031182000043158.

[54] M.M. Basyoni, E.M. Rizk, Nematodes ultrastructure: complex systems and processes, J. Parasit. Dis. 40 (2016) 1130–1140, https://doi.org/10.1007/s12639-015-0707-8.

[55] M.C.K. Leung, J.P. Rooney, I.T. Ryde, A.J. Bernal, A.S. Bess, T.L. Crocker, A. Ji, J. N. Meyer, Effects of early life exposure to ultraviolet C radiation on mitochondrial DNA content, transcription, ATP production, and oxygen consumption in developing *Caenorhabditis elegans*, BMC Pharmacol. Toxicol. 14 (2013) 9, https://doi.org/10.1186/2050-6511-14-9.

[56] H. Peng, J. Jian, H. Long, Q. Jiang, W. Huang, L. Kong, X. Zhang, Y. Li, Z. Liu, J. Chen, T. Wang, F. Zhao, Q. Wu, S. Yan, Self-assembled nanonematicide induces adverse effects on oxidative stress, succinate dehydrogenase activity, and ATP generation, ACS Appl. Mater. Interfaces 15 (2023) 31173–31184, https://doi.org/10.1021/acsami.3c03634[57.

[57] M. Yang, L. Yu, D. Jiang, C. Deng, Z. Wang, X. Xu, Y. Zhang, H. Li, S. Chen, Q. Liu, X. Hu, Calcium stress reduces the reproductive capacity and pathogenicity of the pine wood nematode (*Bursaphelenchus xylophilus*) by inhibiting oxidative phosphorylation reaction, Sci. Total Environ. 912 (2024) 169531, https://doi.org/10.1016/j.scitotenv.2023.169531.